

Phase field modelling of crack propagation, branching and coalescence in rocks

Shuwei Zhou^{3,4}, Xiaoying Zhuang^{4,5}, Hehua Zhu⁴, Timon Rabczuk^{1,2*}

1 Division of Computational Mechanics, Ton Duc Thang University, Ho Chi Minh City, Viet Nam

2 Faculty of Civil Engineering, Ton Duc Thang University, Ho Chi Minh City, Viet Nam

3 Institute of Structural Mechanics, Bauhaus-University Weimar, Weimar 99423, Germany

4 Department of Geotechnical Engineering, College of Civil Engineering, Tongji University, Shanghai 200092, P.R. China

5 Institute of Continuum Mechanics, Leibniz University Hannover, Hannover 30167, Germany

* Corresponding author: timon.rabczuk@tdt.edu.vn

Abstract

We present a phase field model (PFM) for simulating complex crack patterns including crack propagation, branching and coalescence in rock. The phase field model is implemented in COMSOL and is based on the strain decomposition for the elastic energy, which drives the evolution of the phase field. Then, numerical simulations of notched semi-circular bend (NSCB) tests and Brazil splitting tests are performed. Subsequently, crack propagation and coalescence in rock plates with multiple echelon flaws and twenty parallel flaws are studied. Finally, complex crack patterns are presented for a plate subjected to increasing internal pressure, the (3D) Pertersson beam and a 3D NSCB test. All results are in good agreement with previous experimental and numerical results.

Keywords: Phase field, Rock, COMSOL, Crack propagation, Crack branching

1 Introduction

Fracture-induced failure has gained extensive concern in engineering because of the huge threat to engineering safety (Anderson 2005). The prediction of fracture in rock is challenging. Rock masses have many pre-existing flaws, such as micro cracks, voids and soft minerals. Many efforts have been made to study crack propagation in rock, see for instance the contributions in Bobet and Einstein (1998), Wong et al. (2001), Sagong and Bobet (2002), Wong and Einstein (2009), Park and Bobet (2009), Park and Bobet (2010), Lee and Jeon (2011), and Zhou et al. (2014). However, many studies focus on uniaxial compressive loads since tensile loads or more complicated load cases, which are more difficult to perform in practical tests.

Numerical methods are a good alternative to study fracture problems. They are less expensive than experimental tests and can provide physical insight difficult to gain through 'pure' experimental testing. Computational methods for fracture can be classified in discrete and continuous approaches. Efficient remeshing techniques (Areias and Rabczuk 2017, Areias et al. 2013, Areias and Rabczuk 2013), multiscale method (Budarapu et al. 2014a,b, Yang et al. 2015), strain-softening element (Areias et al. 2014), the extended finite element method (Nanthakumar et al. 2014, Moës and Belytschko 2002), the phantom node method (Rabczuk et al. 2008a, Chau-Dinh et al. 2012, Vu-Bac et al. 2013) and specific meshfree methods (Rabczuk et al. 2007a, Rabczuk and Zi 2007, Rabczuk et al. 2007b, 2008a, Rabczuk and Samaniego 2008, Rabczuk et al. 2008b, Amiri et al. 2014a) are classical representatives of the first class. The cracking particles method (CPM) (Rabczuk and Belytschko 2004, 2007, Rabczuk et al. 2010), Peridynamics (Rabczuk and Ren 2017) and dual-horizon peridynamics (Ren et al. 2016, 2017) are also discrete crack approaches but they share the simplicity of continuous approaches to fracture as they also do not require any explicit representation of the crack surface and any crack tracking algorithms. Element-erosion (Belytschko and Lin 1987, Johnson and Stryk 1987) directly sets the stresses of the elements to zero when the elements fulfill the fracture criterion. However, the element-erosion method cannot simulate crack branching correctly (Song et al. 2008). Gradient models (Thai et al. 2016), non-local models (Pijaudier-Cabot et al. 2004), models based on the screened-poisson equation (Areias et al. 2016a) and also phase field models are typical continuous approaches to fracture.

In this paper, we pursue the phase field model (PFM) (Bourdin et al. 2008, Miehe et al. 2010a,b, Hesch and Weinberg 2014, Borden et al. 2012) to model crack propagation, branching and coalescence in rock. The origins of the PFM can be traced back to Bourdin et al. (2008), but a thermodynamic consistent framework was first presented by Miehe et al. (2010a). Considerable attention has been paid to PFMs due to their ease in implementation and applicability to multi-physics problems. The PFM does not treat the crack as a physical discontinuity but uses a scalar field (the phase field) to smoothly transit the intact material to the broken one. Thus, the sharp crack is represented by a 'damage-like' zone. The shape of the crack is controlled by a length scale parameter and propagation of the crack is obtained through the solution of a differential equation. Thus, the PFM does not require any external criterion for fracture and additional work to track the fracture surface algorithmically (Borden et al. 2012). It is believed that for this reason, the phase field is therefore has some advantage over other approaches in modeling branching and merging of multiple cracks.

Phase field models have been discretized in the context of the finite element method (Areias et al. 2016b), meshfree methods (Amiri et al. 2014b) and isogeometric analysis (Borden et al. 2012); the latter two approaches use a fourth-order differential equation for the phase field exploiting the higher continuity of the meshfree and isogeometric approximation. The PFM for brittle cracks has also been implemented in commercial software such as ABAQUS (Msekh et al. 2015, Liu et al. 2016). However, the extension of the implementation in ABAQUS to problems with more fields – as hydraulic fracturing – is difficult. Hence, we present an implementation of the phase field model in COMSOL Multiphysics, a software particularly dedicated to multi-field modeling.

This paper is organized as follows. The phase field model for brittle fractures is presented in Section 2. Subsequently, the numerical implementation of the phase field model in COMSOL is described in Section 3. Then, simulations of initiation, propagation, branching, and coalescence of cracks in rock are shown in Section 4 before Section 5 concludes our manuscript.

2 Theory of phase field modeling

2.1 Theory of brittle fracture

Consider an elastic body $\Omega \subset \mathbb{R}^d$ ($d \in \{1, 2, 3\}$) as shown in Figure 1, whose external boundary and internal discontinuity boundary are denoted as $\partial\Omega$ and Γ , respectively; \mathbf{x} is the position vector and $\mathbf{u}(\mathbf{x}, t) \in \mathbb{R}^d$ the displacement vector at time t . In Fig. 1, the body Ω satisfies the time-dependent Dirichlet boundary conditions ($u_i(\mathbf{x}, t) = g_i(\mathbf{x}, t)$ on $\partial\Omega_{g_i} \in \Omega$), and also the time-dependent Neumann conditions on $\partial\Omega_{h_i} \in \Omega$; $\mathbf{b}(\mathbf{x}, t) \in \mathbb{R}^d$ is the body force and $\mathbf{f}(\mathbf{x}, t)$ the traction on boundary $\partial\Omega_{h_i}$.

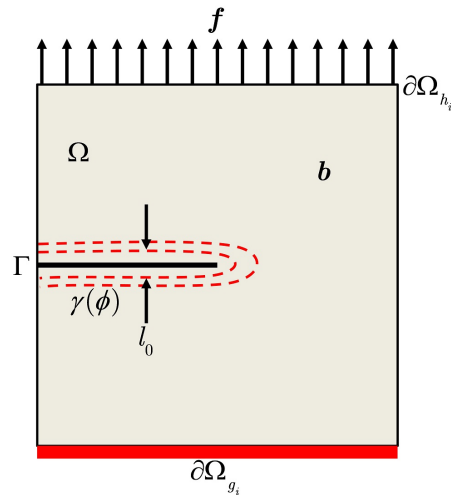


Figure 1: Phase field approximation of the crack surface

Given that the stored elastic energy can be transformed into dissipative forms of energy, the classical Griffith's theory (Anderson 2005) for brittle fracture states that the crack starts to propagate when the stored energy is sufficient to overcome the fracture resistance of the material. Therefore, the crack propagation is regarded as a process to minimize a free energy L that consists of the kinetic energy $\Psi_{kin}(\dot{\mathbf{u}})$, elastic energy Ψ_ε , fracture energy Ψ_f and external work W_{ext} :

$$L = \Psi_{kin}(\dot{\mathbf{u}}) - \underbrace{\int_{\Omega} \psi_\varepsilon(\boldsymbol{\varepsilon}) d\Omega}_{\Psi_\varepsilon} - \underbrace{\int_{\Gamma} G_c dS}_{\Psi_f} + \underbrace{\int_{\Omega} \mathbf{b} \cdot \mathbf{u} d\Omega + \int_{\partial\Omega_{h_i}} \mathbf{f} \cdot \mathbf{u} dS}_{W_{ext}} \quad (1)$$

where $\dot{\mathbf{u}} = \frac{\partial \mathbf{u}}{\partial t}$, ψ_ε is the elastic energy density, and G_c is the critical energy release rate. The linear strain tensor $\boldsymbol{\varepsilon} = \boldsymbol{\varepsilon}(\mathbf{u})$ is given by

$$\boldsymbol{\varepsilon} = \frac{1}{2} [\nabla \mathbf{u} + (\nabla \mathbf{u})^T] \quad (2)$$

The kinetic energy is given by

$$\Psi_{kin}(\dot{\mathbf{u}}) = \frac{1}{2} \int_{\Omega} \rho \dot{\mathbf{u}}^2 d\Omega \quad (3)$$

where ρ indicates the density.

2.2 Phase field approximation for the fracture energy

The phase field method (Miehe et al. 2010a,b, Borden et al. 2012) uses a scalar field, i.e. the phase field, to smear out the crack surface (see Fig. 1) over the domain Ω . The phase field $\phi(\mathbf{x}, t) \in [0, 1]$ has to satisfy the following conditions:

$$\phi = \begin{cases} 0, & \text{if material is intact} \\ 1, & \text{if material is cracked} \end{cases} \quad (4)$$

A typical one dimensional phase field approximated by the exponential function is given by (Miehe et al. 2010a)

$$\phi(x) = e^{-|x|/l_0} \quad (5)$$

l_0 denoting the length scale parameter, which controls the transition region of the phase field and thereby reflects the width of the crack. The distribution of the one dimensional phase field is shown in Fig. 2. The crack region will have a larger width as l_0 increases and the phase field will represent a sharp crack when l_0 tends to zero.

It can be shown that the crack surface density per unit volume of the solid is given by (Miehe et al. 2010a)

$$\gamma(\phi, \nabla \phi) = \frac{\phi^2}{2l_0} + \frac{l_0}{2} |\nabla \phi|^2 \quad (6)$$

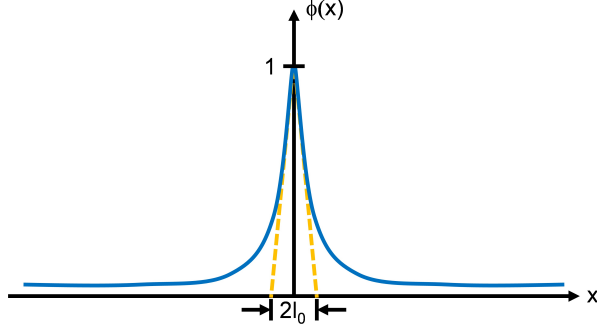


Figure 2: Distribution of the one dimensional phase field across a crack

Thus, the fracture energy is approximated by

$$\int_{\Gamma} G_c dS = \int_{\Omega} G_c \left(\frac{\phi^2}{2l_0} + \frac{l_0}{2} |\nabla \phi|^2 \right) d\Omega \quad (7)$$

The variational approach (Bourdin et al. 2000) states that the crack surface energy is transformed from the elastic energy, which drives the evolution of the phase field. To capture cracks only under tension, the elastic energy is decomposed into tensile and compressive parts (Miehe et al. 2010b):

$$\boldsymbol{\varepsilon}_{\pm} = \sum_{a=1}^d \langle \varepsilon_a \rangle_{\pm} \mathbf{n}_a \otimes \mathbf{n}_a \quad (8)$$

where $\boldsymbol{\varepsilon}_+$ and $\boldsymbol{\varepsilon}_-$ are the tensile and compressive strain tensors, respectively. In addition, ε_a is the principal strain and \mathbf{n}_a is the direction of the principal strain. The operators $\langle \cdot \rangle_{\pm}$ are defined as : $\langle \cdot \rangle_{\pm} = (\cdot \pm |\cdot|)/2$. Consequently, the positive and negative elastic energy densities are expressed as

$$\psi_{\varepsilon}^{\pm}(\boldsymbol{\varepsilon}) = \frac{\lambda}{2} \langle \text{tr}(\boldsymbol{\varepsilon}) \rangle_{\pm}^2 + \mu \text{tr}(\boldsymbol{\varepsilon}_{\pm}^2) \quad (9)$$

where $\lambda > 0$ and $\mu > 0$ are the Lamé constants. The Lamé constants are related to the Young's modulus E and Poisson's ratio ν of the solid through the well known relation:

$$\begin{cases} \lambda = \frac{E\nu}{(1+\nu)(1-2\nu)} \\ \mu = \frac{E}{2(1+\nu)} \end{cases} \quad (10)$$

The phase field is assumed to affect only the positive elastic energy density, which introduces

a stiffness reduction as (Borden et al. 2012)

$$\psi_\varepsilon(\boldsymbol{\varepsilon}) = [(1 - k)(1 - \phi)^2 + k] \psi_\varepsilon^+(\boldsymbol{\varepsilon}) + \psi_\varepsilon^-(\boldsymbol{\varepsilon}) \quad (11)$$

where $0 < k \ll 1$ is a stability parameter for avoiding numerical singularities because the positive elastic energy density disappears as the phase field ϕ tends to 1.

2.3 Governing equations

By substituting Eqs. (3), (7), and (11) into Eq. (1), the energy functional L is rewritten as

$$L = \frac{1}{2} \int_{\Omega} \rho \dot{\mathbf{u}}^2 d\Omega - \int_{\Omega} \{ [(1 - k)(1 - \phi)^2 + k] \psi_\varepsilon^+(\boldsymbol{\varepsilon}) + \psi_\varepsilon^-(\boldsymbol{\varepsilon}) \} d\Omega - \int_{\Omega} G_c \left(\frac{\phi^2}{2l_0} + \frac{l_0}{2} |\nabla \phi|^2 \right) d\Omega + \int_{\Omega} \mathbf{b} \cdot \mathbf{u} d\Omega + \int_{\partial\Omega_{h_i}} \mathbf{f} \cdot \mathbf{u} dS \quad (12)$$

Employ the first variation of the functional $\delta L = 0$, it can be shown that the strong form of the governing equations are given by (Borden et al. 2012)

$$\left\{ \begin{array}{l} \text{Div}(\boldsymbol{\sigma}) + \mathbf{b} = \rho \ddot{\mathbf{u}} \\ \left[\frac{2l_0(1 - k)\psi_\varepsilon^+}{G_c} + 1 \right] \phi - l_0^2 \nabla^2 \phi = \frac{2l_0(1 - k)\psi_\varepsilon^+}{G_c} \end{array} \right. \quad (13)$$

where $\ddot{\mathbf{u}} = \frac{\partial^2 \mathbf{u}}{\partial t^2}$ and $\boldsymbol{\sigma}$ is Cauchy stress tensor given by

$$\begin{aligned} \boldsymbol{\sigma} &= \partial_{\boldsymbol{\varepsilon}} \psi_\varepsilon \\ &= [(1 - k)(1 - \phi)^2 + k] [\lambda \langle \text{tr}(\boldsymbol{\varepsilon}) \rangle_+ \mathbf{I} + 2\mu \boldsymbol{\varepsilon}_+] + \lambda \langle \text{tr}(\boldsymbol{\varepsilon}) \rangle_- \mathbf{I} + 2\mu \boldsymbol{\varepsilon}_- \end{aligned} \quad (14)$$

with unit tensor $\mathbf{I} \in \mathbb{R}^{d \times d}$.

The phase field requires the irreversibility condition $\Gamma(\mathbf{x}, s) \in \Gamma(\mathbf{x}, t) (s < t)$ during compression or unloading, i.e. the crack cannot be healed. Therefore, we introduce a strain-history field $H(\mathbf{x}, t)$ (Miehe et al. 2010a,b) to ensure a monotonically increasing phase field:

$$H(\mathbf{x}, t) = \max_{s \in [0, t]} \psi_\varepsilon^+(\boldsymbol{\varepsilon}(\mathbf{x}, s)) \quad (15)$$

The history field H satisfies the Kuhn-Tucker conditions for loading and unloading (Miehe et al. 2010a):

$$\psi_\varepsilon^+ - H \leq 0, \quad \dot{H} \geq 0, \quad \dot{H}(\psi_\varepsilon^+ - H) = 0 \quad (16)$$

By replacing ψ_ε^+ by $H(\mathbf{x}, t)$ in Eq. (13), the strong form is rewritten as

$$\left\{ \begin{array}{l} \text{Div}(\boldsymbol{\sigma}) + \mathbf{b} = \rho \ddot{\mathbf{u}} \\ \left[\frac{2l_0(1-k)H}{G_c} + 1 \right] \phi - l_0^2 \nabla^2 \phi = \frac{2l_0(1-k)H}{G_c} \end{array} \right. \quad (17)$$

We denote \mathbf{m} as the outward-pointing normal vector to the boundaries, and the governing equations are subjected to the Dirichlet and Neumann boundary conditions

$$\left\{ \begin{array}{ll} \mathbf{u} = \mathbf{g} & \text{on } \partial\Omega_{g_i} \\ \boldsymbol{\sigma} \cdot \mathbf{m} = \mathbf{f} & \text{on } \partial\Omega_{h_i} \\ \nabla \phi \cdot \mathbf{m} = 0 & \text{on } \partial\Omega \end{array} \right. \quad (18)$$

along with the initial conditions

$$\left\{ \begin{array}{ll} \mathbf{u}(\mathbf{x}, 0) = \mathbf{u}_0(\mathbf{x}) & \mathbf{x} \in \Omega \\ \mathbf{v}(\mathbf{x}, 0) = \mathbf{v}_0(\mathbf{x}) & \mathbf{x} \in \Omega \\ \phi(\mathbf{x}, 0) = \phi_0(\mathbf{x}) & \mathbf{x} \in \Omega \end{array} \right. \quad (19)$$

2.4 The choice of l_0

Borden et al. (2012) and Zhang et al. (2017) proposed an analytical solution for the critical tensile stress σ_{cr} that a one-dimensional bar can sustain:

$$\sigma_{cr} = \frac{9}{16} \sqrt{\frac{EG_c}{3l_0}} \quad (20)$$

There is an apparent singularity when l_0 tends to zero, i.e. in case of a sharp crack, which is physically meaningless. However, assuming all other parameters except of l_0 are known, eq.

(20) can be solved for l_0 :

$$l_0 = \frac{27EG_c}{256\sigma_{cr}^2} \quad (21)$$

In Eq. (21), the critical energy release rate G_c and Young's modulus E can be obtained by conducting regular experimental tests, while the critical stress σ_{cr} can be approximated by the tensile strength σ_t through the standard tensile test. Hence, Eq. (21) can estimate the length scale. Note that the accuracy is unknown for more complex cases.

3 Numerical implementation

3.1 Finite element method

We use the finite element method to solve the governing equations (17) given in weak form by

$$\int_{\Omega} (-\rho\ddot{\mathbf{u}} \cdot \delta\mathbf{u} - \boldsymbol{\sigma} : \delta\boldsymbol{\varepsilon}) d\Omega + \int_{\Omega} \mathbf{b} \cdot \delta\mathbf{u} d\Omega + \int_{\Omega_{h_i}} \mathbf{f} \cdot \delta\mathbf{u} dS = 0 \quad (22)$$

and

$$\int_{\Omega} -2(1-k)H(1-\phi)\delta\phi d\Omega + \int_{\Omega} G_c \left(l_0 \nabla\phi \cdot \nabla\delta\phi + \frac{1}{l_0} \phi\delta\phi \right) d\Omega = 0 \quad (23)$$

We use the standard vector-matrix notation and denote the nodal values of the displacement and phase field as \mathbf{u}_i and ϕ_i . The discretization is thereby given by

$$\mathbf{u} = \mathbf{N}_u \mathbf{d}, \quad \phi = \mathbf{N}_\phi \hat{\boldsymbol{\phi}} \quad (24)$$

where \mathbf{d} and $\hat{\boldsymbol{\phi}}$ are the vectors consisting of node values \mathbf{u}_i and ϕ_i . \mathbf{N}_u and \mathbf{N}_ϕ are shape function matrices given by

$$\mathbf{N}_u = \begin{bmatrix} N_1 & 0 & 0 & \dots & N_n & 0 & 0 \\ 0 & N_1 & 0 & \dots & 0 & N_n & 0 \\ 0 & 0 & N_1 & \dots & 0 & 0 & N_n \end{bmatrix}, \quad \mathbf{N}_\phi = \begin{bmatrix} N_1 & N_2 & \dots & N_n \end{bmatrix} \quad (25)$$

where n is the node number in one element and N_i is the shape function of node i . The same

discretization is applied to the test functions and we obtain

$$\delta \mathbf{u} = \mathbf{N}_u \delta \mathbf{d}, \quad \delta \phi = \mathbf{N}_\phi \delta \hat{\phi} \quad (26)$$

where $\delta \mathbf{d}$ and $\delta \hat{\phi}$ are the vectors consisting of node values of the test functions.

The gradients are thereby calculated by

$$\boldsymbol{\varepsilon} = \mathbf{B}_u \mathbf{d}, \quad \nabla \phi = \mathbf{B}_\phi \hat{\phi}, \quad \delta \boldsymbol{\varepsilon} = \mathbf{B}_u \delta \mathbf{d}, \quad \nabla \delta \phi = \mathbf{B}_\phi \delta \hat{\phi} \quad (27)$$

where \mathbf{B}_u and \mathbf{B}_ϕ are the derivatives of the shape functions defined by

$$\mathbf{B}_u = \begin{bmatrix} N_{1,x} & 0 & 0 & \dots & N_{n,x} & 0 & 0 \\ 0 & N_{1,y} & 0 & \dots & 0 & N_{n,y} & 0 \\ 0 & 0 & N_{1,z} & \dots & 0 & 0 & N_{n,z} \\ N_{1,y} & N_{1,x} & 0 & \dots & N_{n,y} & N_{n,x} & 0 \\ 0 & N_{1,z} & N_{1,y} & \dots & 0 & N_{n,z} & N_{n,y} \\ N_{1,z} & 0 & N_{1,x} & \dots & N_{n,z} & 0 & N_{n,x} \end{bmatrix}, \quad \mathbf{B}_\phi = \begin{bmatrix} N_{1,x} & N_{2,x} & \dots & N_{n,x} \\ N_{1,y} & N_{2,y} & \dots & N_{n,y} \\ N_{1,z} & N_{2,z} & \dots & N_{n,z} \end{bmatrix} \quad (28)$$

By applying the finite element approximation, the equations of weak form (22) and (23) are then written as

$$- (\delta \mathbf{d})^T \left[\int_{\Omega} \rho \mathbf{N}_u^T \mathbf{N}_u d\Omega \ddot{\mathbf{d}} + \int_{\Omega} \mathbf{B}_u^T \mathbf{D}_e \mathbf{B}_u d\Omega \mathbf{d} \right] + (\delta \mathbf{d})^T \left[\int_{\Omega} \mathbf{N}_u^T \mathbf{b} d\Omega + \int_{\Omega_{h_i}} \mathbf{N}_u^T \mathbf{f} dS \right] = 0 \quad (29)$$

$$- (\delta \hat{\phi})^T \int_{\Omega} \left\{ \mathbf{B}_\phi^T G_c l_0 \mathbf{B}_\phi + \mathbf{N}_\phi^T \left[\frac{G_c}{l_0} + 2(1-k)H \right] \mathbf{N}_\phi \right\} d\Omega \hat{\phi} + (\delta \hat{\phi})^T \int_{\Omega} 2(1-k)H \mathbf{N}_\phi^T d\Omega = 0 \quad (30)$$

where \mathbf{D}_e is the degraded stiffness matrix. \mathbf{D}_e can be calculated from the fourth order elasticity tensor \mathbf{D} :

$$\begin{aligned} \mathbf{D} &= \frac{\partial \boldsymbol{\sigma}}{\partial \boldsymbol{\varepsilon}} \\ &= \lambda \left\{ [(1-k)(1-\phi)^2 + k] H_\varepsilon(\text{tr}(\boldsymbol{\varepsilon})) + H_\varepsilon(-\text{tr}(\boldsymbol{\varepsilon})) \right\} \mathbf{J} + 2\mu \left\{ [(1-k)(1-\phi)^2 + k] \mathbf{P}^+ + \mathbf{P}^- \right\} \end{aligned} \quad (31)$$

where $J_{ijkl} = \delta_{ij}\delta_{kl}$, δ_{ij} being the Kronecker and $P_{ijkl}^\pm = \sum_{a=1}^3 \sum_{b=1}^3 H_\varepsilon(\varepsilon_a)\delta_{ab}n_{ai}n_{aj}n_{bk}n_{bl} + \sum_{a=1}^3 \sum_{b \neq a}^3 \frac{1}{2} \frac{\langle \varepsilon_a \rangle \pm \langle \varepsilon_b \rangle}{\varepsilon_a - \varepsilon_b} n_{ai}n_{bj}(n_{ak}n_{bl} + n_{bk}n_{al})$ with n_{ai} the i -th component of vector \mathbf{n}_a ; $H_\varepsilon\langle x \rangle$ is the Heaviside function:

$$H_\varepsilon\langle x \rangle = \begin{cases} 1, & x > 0 \\ 0, & x \leq 0 \end{cases} \quad (32)$$

Since P_{ijkl}^\pm cannot be computed when $\varepsilon_a = \varepsilon_b$, we apply a ‘‘perturbation’’ technology for the principal strains (Miehe 1993) with an unchanged ε_2 :

$$\begin{cases} \varepsilon_1 = \varepsilon_1(1 + \delta) & \text{if } \varepsilon_1 = \varepsilon_2 \\ \varepsilon_3 = \varepsilon_3(1 - \delta) & \text{if } \varepsilon_2 = \varepsilon_3 \end{cases} \quad (33)$$

with the perturbation $\delta = 1 \times 10^{-9}$.

For admissible arbitrary test functions, Eqs. (29) and (30) always hold, thereby producing the discretized weak form as

$$-\underbrace{\int_{\Omega} \rho \mathbf{N}_u^T \mathbf{N} d\Omega \ddot{\mathbf{d}}}_{\mathbf{F}_u^{ine} = \mathbf{M} \ddot{\mathbf{d}}} - \underbrace{\int_{\Omega} \mathbf{B}_u^T \mathbf{D}_e \mathbf{B}_u d\Omega \mathbf{d}}_{\mathbf{F}_u^{int} = \mathbf{K}_u \mathbf{d}} + \underbrace{\int_{\Omega} \mathbf{N}_u^T \mathbf{b} d\Omega + \int_{\Omega_{h_i}} \mathbf{N}_u^T \mathbf{f} dS}_{\mathbf{F}_u^{ext}} = 0 \quad (34)$$

$$-\underbrace{\int_{\Omega} \left\{ \mathbf{B}_\phi^T G_c l_0 \mathbf{B}_\phi + \mathbf{N}_\phi^T \left[\frac{G_c}{l_0} + 2(1-k)H \right] \mathbf{N}_\phi \right\} d\Omega \hat{\phi}}_{\mathbf{F}_\phi^{int} = \mathbf{K}_\phi \hat{\phi}} + \underbrace{\int_{\Omega} 2(1-k)H \mathbf{N}_\phi^T d\Omega}_{\mathbf{F}_\phi^{ext}} = 0 \quad (35)$$

where \mathbf{F}_u^{ine} , \mathbf{F}_u^{int} , and \mathbf{F}_u^{ext} are the inertial, internal, and external forces for the displacement field and \mathbf{F}_ϕ^{int} and \mathbf{F}_ϕ^{ext} are the internal and external force terms of the phase field. In addition, the mass and stiffness matrices follow

$$\begin{cases} \mathbf{M} = \int_{\Omega} \rho \mathbf{N}_u^T \mathbf{N} d\Omega \\ \mathbf{K}_u = \int_{\Omega} \mathbf{B}_u^T \mathbf{D}_e \mathbf{B}_u d\Omega \\ \mathbf{K}_\phi = \int_{\Omega} \left\{ \mathbf{B}_\phi^T G_c l_0 \mathbf{B}_\phi + \mathbf{N}_\phi^T \left[\frac{G_c}{l_0} + 2(1-k)H \right] \mathbf{N}_\phi \right\} d\Omega \end{cases} \quad (36)$$

In this paper, we use a staggered scheme to solve the displacement and phase fields. Thus, the Newton-Raphson approach is adopted to obtain the residual of the discrete equations $\mathbf{R}_u =$

$\mathbf{F}_u^{ext} - \mathbf{F}_u^{ine} - \mathbf{F}_u^{int} = 0$ and $\mathbf{R}_\phi = \mathbf{F}_\phi^{ext} - \mathbf{F}_\phi^{int} = 0$, respectively.

3.2 COMSOL implementation

We implemented the phase field approach into COMSOL Multiphysics, which can simulate mathematical and physical problems easily by adding application-specific modules. Therefore, it is suitable for multi-field modeling. In this paper, we construct three main modules, namely, the Solid Mechanics, History-strain and Phase Field Modules, which employ the standard finite element discretization in space as described in Subsection 3.1. In addition, a pre-set Storage Module is employed to evaluate and store the intermediate field variables in a time step, such as the positive elastic energy and principal strains.

Based on a linear elastic material library, the Solid Mechanics Module is used for the displacement \mathbf{u} . The boundary and initial conditions shown in Section 2 are added to the Solid Mechanics Module, while a non-linear stress-strain relationship is considered. The stiffness matrix D_e is modified in a time step as follows

$$\mathbf{D}_e = \begin{bmatrix} D_{1111} & D_{1122} & D_{1133} & D_{1112} & D_{1123} & D_{1113} \\ D_{2211} & D_{2222} & D_{2233} & D_{2212} & D_{2223} & D_{2213} \\ D_{3311} & D_{3322} & D_{3333} & D_{3312} & D_{3323} & D_{3313} \\ D_{1211} & D_{1222} & D_{1233} & D_{1212} & D_{1223} & D_{1213} \\ D_{2311} & D_{2322} & D_{2333} & D_{2312} & D_{2323} & D_{2313} \\ D_{1311} & D_{1322} & D_{1333} & D_{1312} & D_{1323} & D_{1313} \end{bmatrix} \quad (37)$$

The governing equation (17) is presented for dynamic crack problems. However, for a quasi-static problem, the inertia term must be neglected in the Solid Mechanics Module. The Phase Field Module is established for the phase field ϕ by revising a pre-defined module, which is governed by the Helmholtz equation. The boundary condition Eq. (18) and initial condition (19) are also implemented in this module. For the history strain field H , the Distributed ODEs and DAEs Interfaces are used to construct the History-strain Module, where the history strain field is not solved directly. We use a “previous solution” solver to record the results in the

previous time steps and obtain the field H by applying the following format in COMSOL:

$$\begin{cases} H - \psi_\varepsilon^+ = 0, & \text{if } \psi_\varepsilon^+ > H \\ H - H = 0, & \text{if } \psi_\varepsilon^+ \leq H \end{cases} \quad (38)$$

Additionally, the initial condition $H_0(\mathbf{x}) = 0$ is used for the History-strain Module.

Figure 3 shows the relationship among all the established modules. The mechanical responses, such as the principal strains, the directions of principal strain, and the elastic energy, are naturally exported from the Solid Mechanics Module and stored in the Storage Module. The History-strain Module then call the positive elastic energy and update the local history strain field H . The Phase Field Module employs the updated H to solve the phase field. In a time step, the updated phase field and the stored principal strains as well as the directions are used to modify the stiffness matrix of the Solid Mechanics Module and subsequently to obtain the mechanical responses.

The detailed procedure of the staggered (segregated) scheme is depicted in Fig. 4. The equations of displacement, history strain and phase-field are solved independently. An implicit Generalized- α method (Borden et al. 2012) is used for time integration. The Generalized- α method is unconditionally stable and requires a prediction step and a correction step. When a new time step starts, an initial guess from the linear extrapolation of the previous solution is used in the prediction stage. Newton-Raphson iterations are used to solve the residuals for each module in the correction stage. That is, in the iteration step $j + 1$ of a given time step i , the displacement \mathbf{u}_i^{j+1} is first solved by using the results $(\mathbf{u}_i^j, H_i^j \text{ and } \phi_i^j)$ of the previous iteration step j . Following the updated displacements \mathbf{u}_i^{j+1} , the history strain is updated. Subsequently, another Newton-Raphson iteration is applied to solve the phase-field ϕ_i^{j+1} . The total relative error is estimated and the iterations continue until the tolerance requirement is met. The maximum number of iteration in one time step is set as 50 in our simulations. We accelerate the convergence by using the Anderson acceleration (Toth and Kelley 2015) where the dimension of the iteration space field is chosen as more than 50. A flow chart of our implementation is shown in Fig. 5. The source code can be found in “<https://sourceforge.net/projects/phasefieldmodelingcomsol/>”.

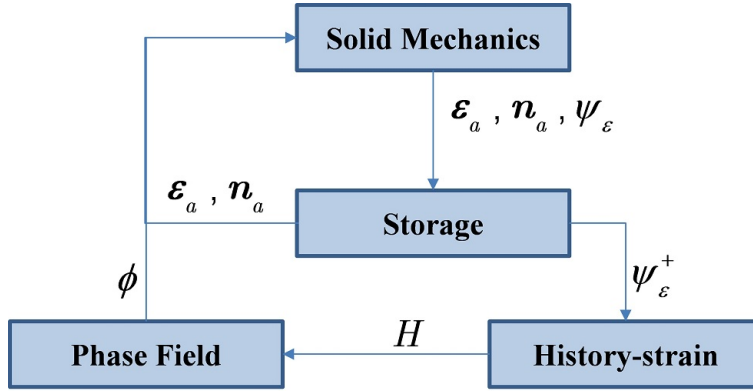


Figure 3: Relationship between all the modules established

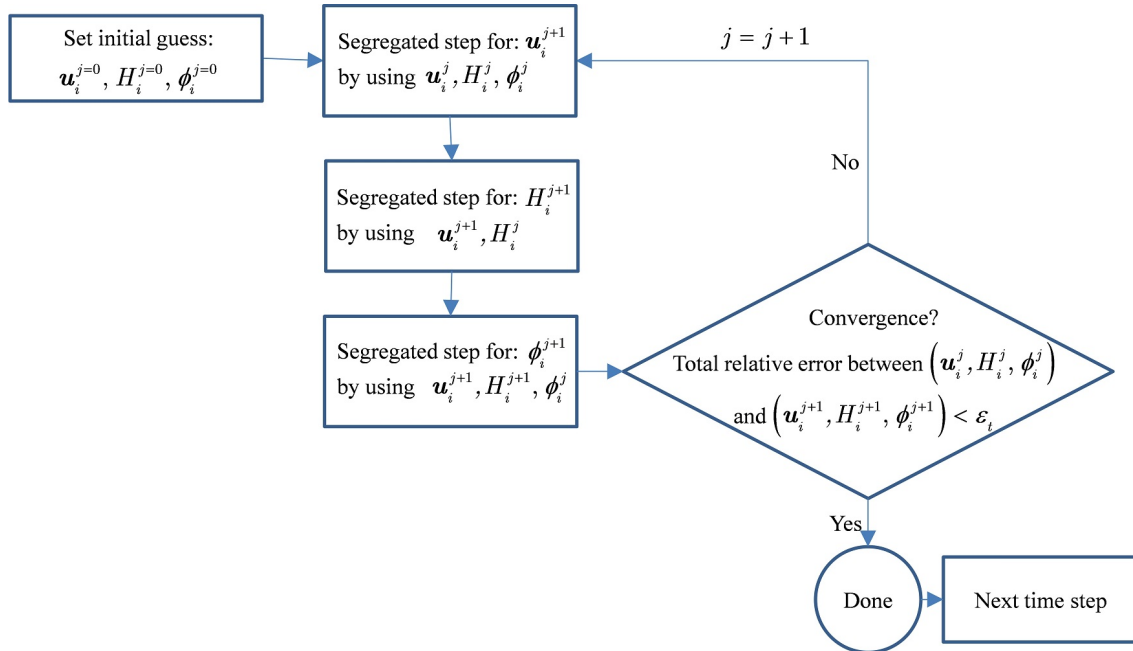


Figure 4: Segregated scheme for the coupled calculation in phase field modeling

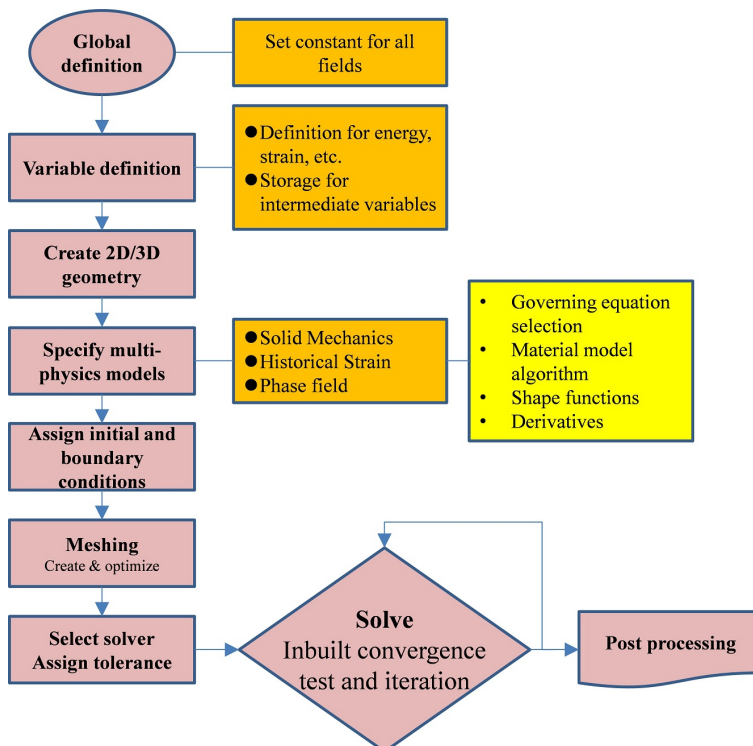


Figure 5: COMSOL implementation of the phase field modeling

4 Numerical examples of crack propagation, branching and coalescence in rocks

4.1 Simulation of notched semi-circular bend (NSCB) tests

Let us consider the notched semi-circular bend (NSCB) test first. Geometry and boundary condition of the rock specimen are shown in Fig.6. The mechanical properties of the rock are taken from the Laurentian granite (LG) from Grenville province of Canada (Gao et al. 2015). The rock density ρ is 2630 kg/m^3 , while the Young's modulus E and Poisson's ratio ν are 92 GPa and 0.21, respectively. We follow the 1D solution of Borden et al. (2012) for the critical stress of material softening, and choose $G_c = 7.6 \text{ J/m}^2$ and the length scale $l_0 = 4.5 \times 10^{-4} \text{ m}$. This produces a critical stress close to the quasi-static tensile strength of the specimen (12.8 MPa) (Gao et al. 2015).

The phase field modeling is performed by using 93587 6-node quadratic triangular elements and the maximum element size is $h = 2.25 \times 10^{-4} \text{ m}$. We apply a vertical displacement on the

top of the specimen to drive crack propagation from the tip of the notch. During the simulation, we apply the displacement increment $\Delta u = 5 \times 10^{-7}$ mm in each time step.

Figure 7 shows the crack initiation and propagation in the rock specimen by using the phase field model. When the applied displacement u reaches to 6.72×10^{-3} mm, the crack initiates from the tip of the notch. Subsequently, the crack propagates straightly in the vertical direction when u accumulates to 6.74×10^{-3} mm and 6.77×10^{-3} mm. When the displacement reaches to 6.86×10^{-3} mm, the tip of the propagating crack is close to the upper boundary of the specimen and failure of the semi-circular rock specimen occurs. The crack patterns obtained by the phase field simulation are in good agreement with the experimental results in Gao et al. (2015).

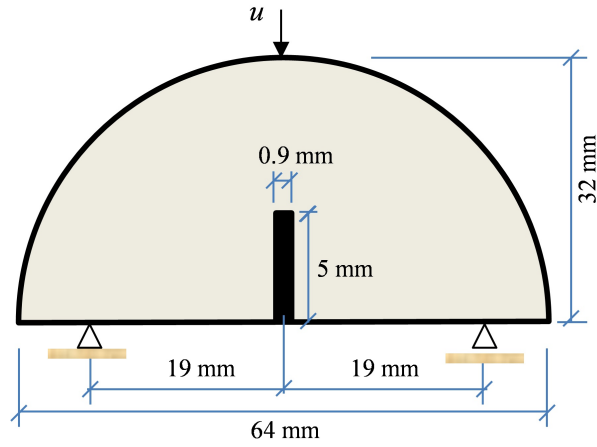


Figure 6: Geometry and boundary condition of the notched semi-circular bend (NSCB) tests

We test the crack patterns for $G_c = 5.6, 6.6, 8.6,$ and 9.6 J/m². The results show that G_c has little influence on the crack patterns. Different G_c have the same crack paths. Figure 8 gives the curves of the reaction force on the upper boundary of the specimen versus the displacement for different G_c . A sudden drop of the load is observed after the crack initiation. In addition, all the curves have the same slope before the crack initiation under different G_c , while the maximum load increases as G_c increases .

We also test the influence of the maximum mesh size h under a fixed $G_c = 7.6$ J/m² and the length scale $l_0 = 4.5 \times 10^{-4}$ m. We choose $h = 2.25 \times 10^{-4}$ m, 1.13×10^{-4} m, and 5.63×10^{-5} m in the tests. The resulting load-displacement curve is shown in Fig. 9. As expected, the load-displacement curve converges with the mesh refinement. To test the influence of the length scale l_0 , we fix the mesh size $h = 2.25 \times 10^{-4}$ m and $G_c = 7.6$ J/m², and then present the

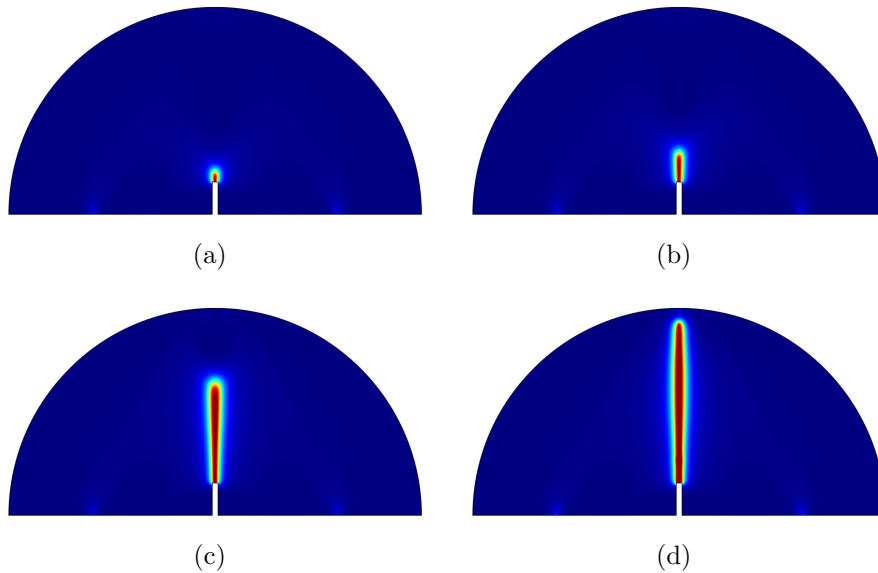


Figure 7: Crack propagation of the notched semi-circular bend (NSCB) tests at a displacement of (a) $u = 6.72 \times 10^{-3}$ mm, (b) $u = 6.77 \times 10^{-3}$ mm, (c) $u = 6.74 \times 10^{-3}$ mm, and (d) $u = 6.86 \times 10^{-3}$ mm for $G_c = 7.6$ J/m²

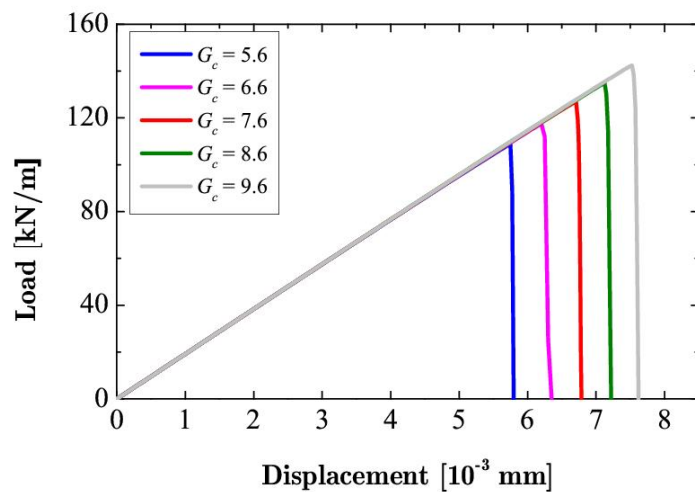


Figure 8: Load-displacement curves of the notched semi-circular bend (NSCB) tests

load-displacement curve for different l_0 in Fig. 10. Figure 10 shows a decreasing peak load and displacement range when the length scale increases.

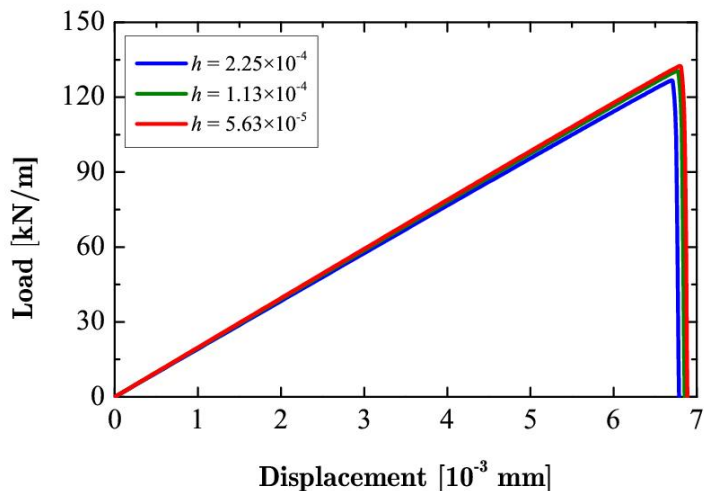


Figure 9: Load-displacement curves of the NSCB tests under different mesh size

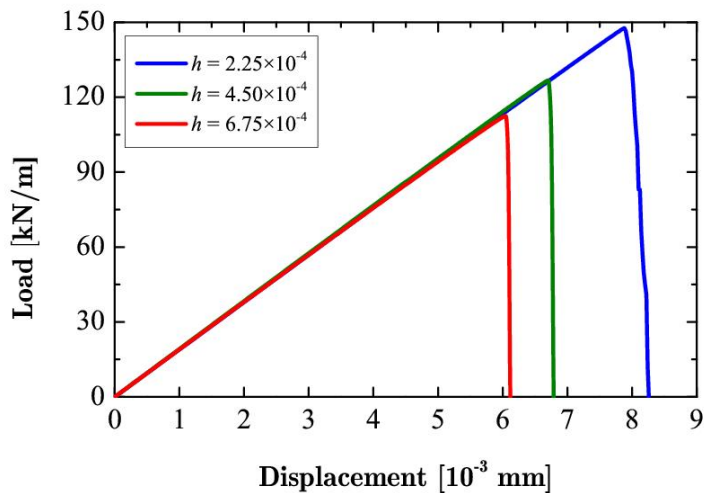


Figure 10: Load-displacement curves of the NSCB tests under different length scale l_0

4.2 Simulation of Brazil splitting tests

Brazil splitting tests are commonly used to obtain the tensile strength of rocks and many researchers simulated crack propagation in a Brazilian disc under compression, such as Cai (2013)

and Zhou and Wang (2016). Figure 11 presents the geometry of the Brazilian disc along with the boundary conditions.

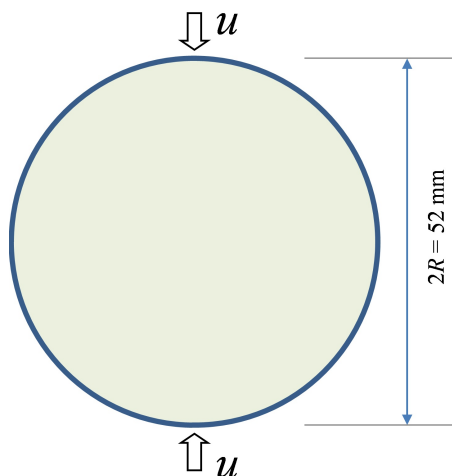


Figure 11: Geometry and boundary condition of the Brazil splitting tests

These material parameters are adopted: $\rho = 2630 \text{ kg/m}^3$, $E = 31.5 \text{ GPa}$, and $\nu = 0.25$. The length scale parameter l_0 is fixed to 1 mm. 26700 linear triangular elements (base mesh) are used to discretize the disc with the maximum element size $h = 0.5 \text{ mm}$, k is set to 1×10^{-9} . Finally, we conduct the simulation by using five different G_c : 50, 75, 100, 125, and 150 J/m².

Figure 12 shows the crack initiation and propagation in the Brazil splitting tests for $G_c = 100 \text{ J/m}^2$. When the displacement u approaches a value of 0.476 mm, the crack occurs in the center of the disc where the maximum tensile stress occurs which is in good agreement with the experimental and analytical results (Atkinson et al. 1982, Entacher et al. 2015). When u reaches a value of 0.477 mm, the crack propagates with an increasing width. Then, the crack continues to propagate and the crack tips move close to the upper and bottom ends of the disc when u reaches to 0.478 mm. The crack branching is observed when u is close to 0.480 mm. In addition, the crack cannot penetrate deeply into the ends of the disc because of the locally compressed area around both ends.

We compare the curve of the reaction force on the upper end of the Brazilian disc versus the displacement u with the experimental result in Fig. 13. The experimental curve is originated from the work of Erarslan and Williams (2012). Figure 13 shows that the phase field model can reproduce the experimental results well. The main reason for the difference in Fig. 13 is

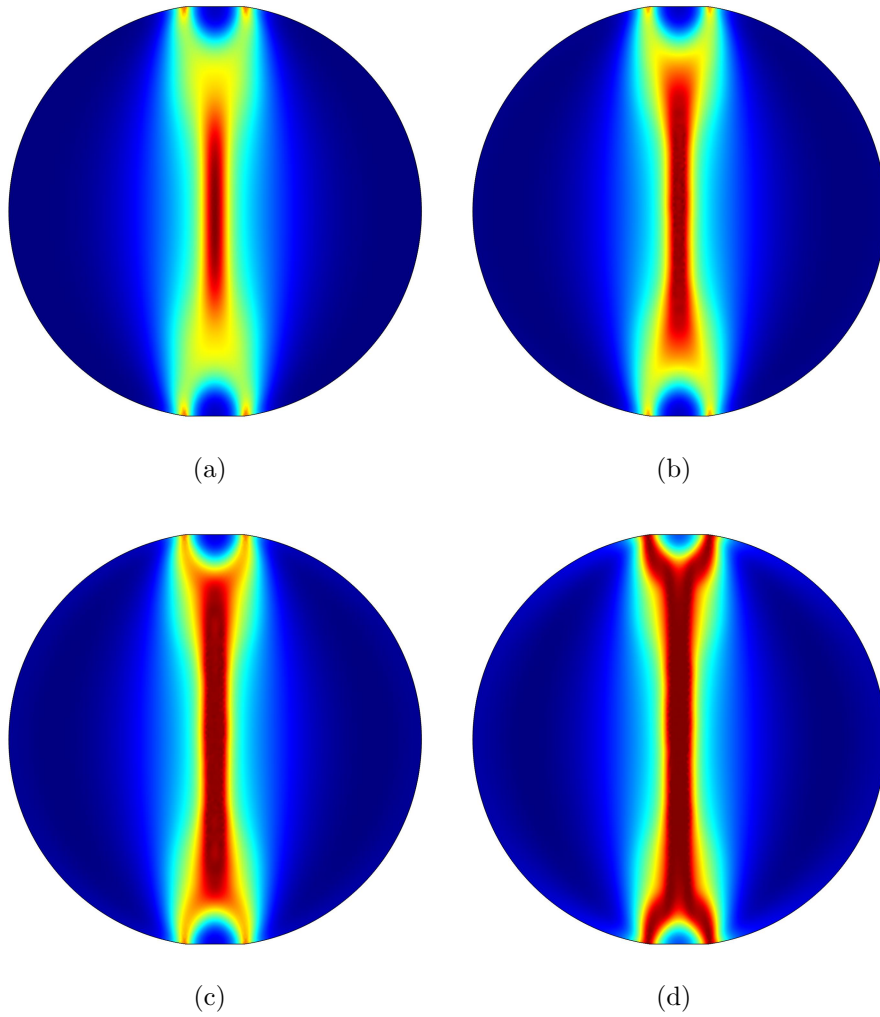


Figure 12: Crack propagation of the Brazil splitting tests at a displacement of (a) $u = 0.476$ mm, (b) $u = 0.477$ mm, (c) $u = 0.478$ mm, and (d) $u = 0.480$ mm for $G_c = 100$ J/m²

that there are contact issues in the actual Brazilian tests and a compaction stage is commonly observed before the elastic stage.

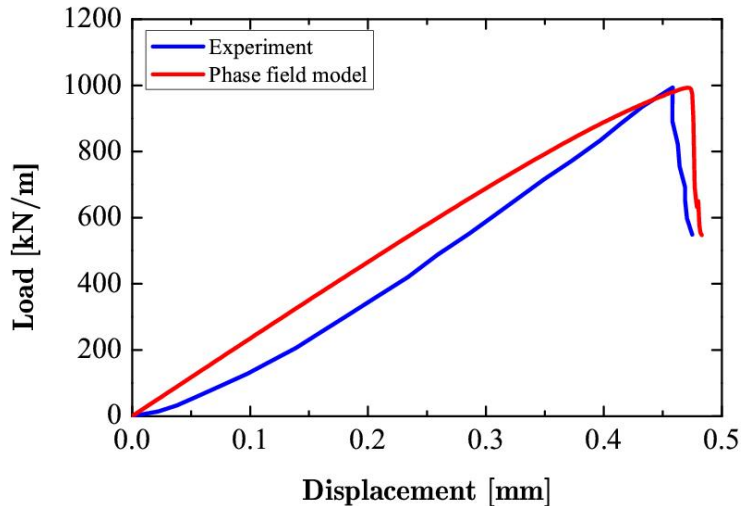


Figure 13: Comparison of the load-displacement curves obtained by the experimental test and phase field modeling

Figure 14 presents the curves of the reaction force on the upper end of the Brazilian disc versus the displacement u for different G_c . Similar to the NSCB tests, a sudden drop of the load is observed after the phase field increases to 1. In addition, the peak load increases with the increase in G_c . We then test the influence of the length scale l_0 under a fixed $G_c = 100 \text{ J/m}^2$ and mesh size $h = 0.5 \text{ mm}$. The tested length scale parameters are $l_0 = 0.5, 1, 2, \text{ and } 3 \text{ mm}$, respectively. The load-displacement curves under different length scale l_0 are shown in Fig. 15. As shown in Fig. 15, the peak load of the specimen decreases with the increase in the length scale l_0 .

We also test the influence of mesh size h under a fixed $G_c = 100 \text{ J/m}^2$ and $l_0 = 1 \text{ mm}$. The maximum mesh size h is set as 1, 0.5, 0.25, and 0.125 m, respectively. The resulting load-displacement curve is shown in Fig. 16. The load-displacement curve converges with mesh refinement as expected. In addition, in the Brazil splitting test, the tensile strength σ_t of the rock specimen is given by

$$\sigma_t = \frac{2P_{peak}}{\pi DL} \quad (39)$$

where P_{peak} is the peak load, and D and L are the diameter and length of the rock specimen. Thus, we compare the tensile strength by the phase field simulation and the critical stress for

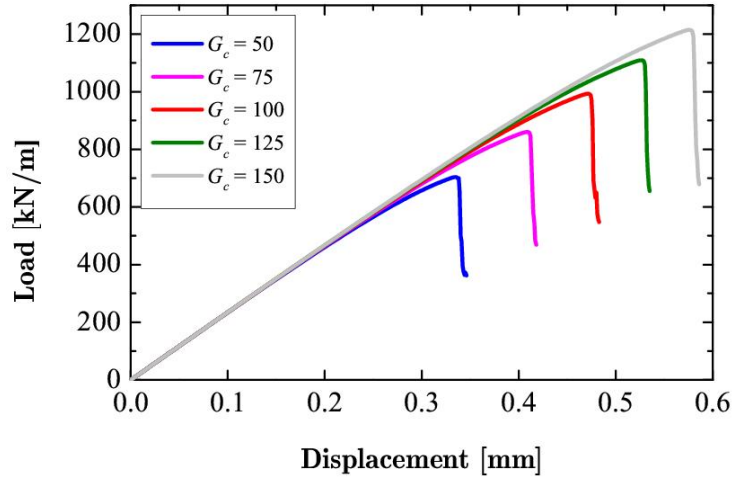


Figure 14: Load-displacement curves for the Brazil splitting tests for different G_c

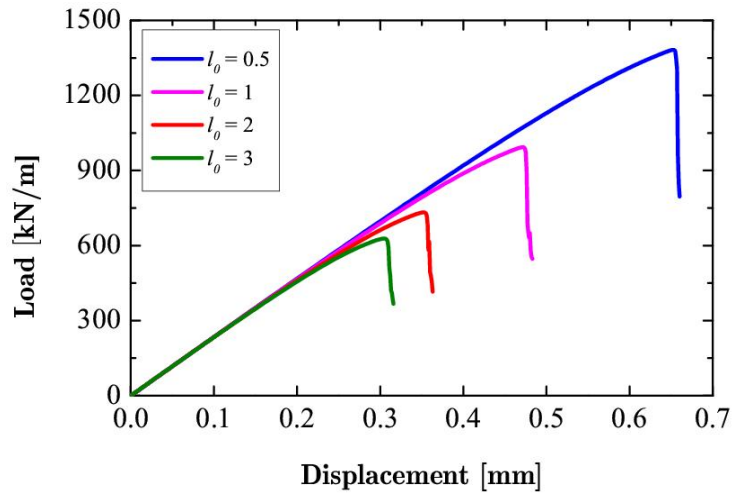


Figure 15: Load-displacement curves for the Brazil splitting tests for different l_0

1D by Borden et al. (2012) in Fig. 17. The tensile strength increases at a decreasing rate with the increase in G_c . The critical stress has the same trend as the tensile strength. However, the critical stress is far larger than the tensile strength. This observation indicates that the critical stress for 1D analysis cannot be applied directly to 2D or 3D.

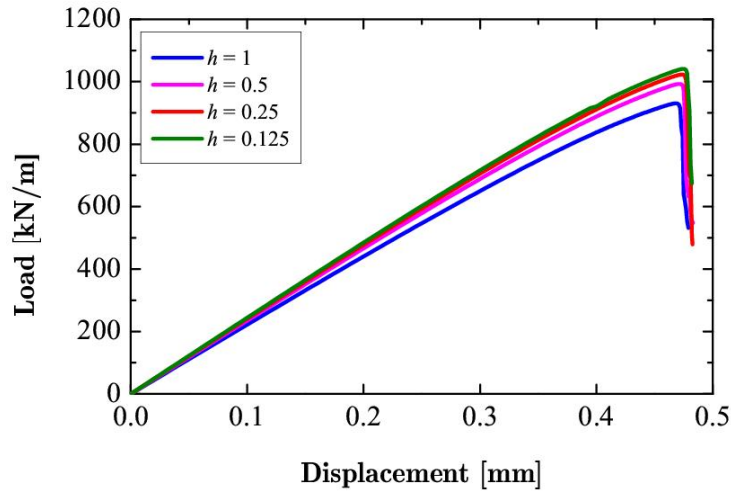


Figure 16: Load-displacement curves for the Brazil splitting tests for different h

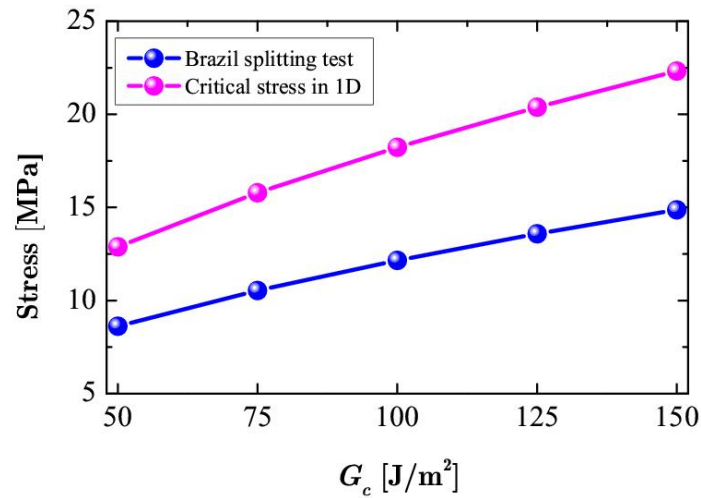


Figure 17: Comparison of tensile strength by Brazil splitting tests and critical stress for 1D

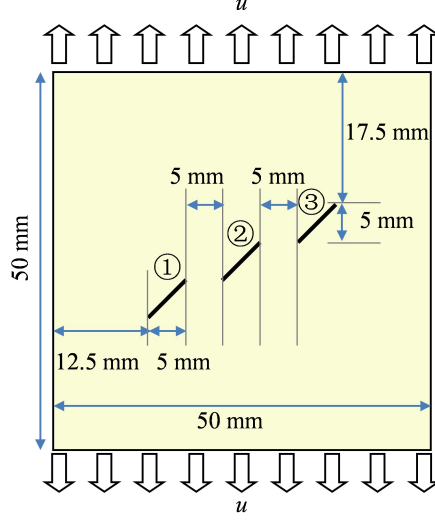


Figure 18: Geometry and boundary condition of three pre-existing flaws

4.3 Propagation of multiple echelon flaws

We consider a 50 mm \times 50 mm square rock sample subjected to tension. The rock sample has three pre-existing flaws, whose position and geometry are shown in Fig. 18. All the flaws have the same length, spacing, and inclination angle of 45°. These parameters are adopted: the rock density $\rho = 2500 \text{ kg/m}^3$, the Young's modulus $E = 30 \text{ GPa}$, the Poisson's ratio $\nu = 0.333$, $G_c = 3 \text{ J/m}^2$, $k = 1 \times 10^{-5}$, and the length scale $l_0 = 0.25 \text{ mm}$. Vertical displacements are applied on the top and bottom boundaries of the rock sample as shown in Fig. 18. The simulation is performed by using 106852 6-node quadratic triangular elements where the maximum element size h is 0.25 mm. In each time step, the displacement increment is $\Delta u = 5 \times 10^{-7} \text{ mm}$.

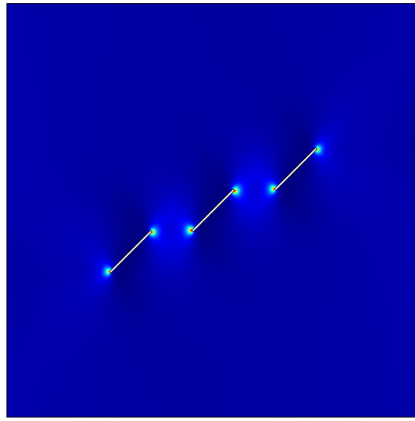
Figure 19(a)-(f) shows the propagation and coalescence of the three pre-existing flaws. We also calculate the reaction force on the upper boundary of the rock sample, and present the load-displacement curves in Fig. 20. As the displacement u increases, both the load and the phase field around the tips of the flaws increase. When u reaches to $2.6 \times 10^{-3} \text{ mm}$, the phase field increases close to 1 and the load approaches to the maximum value. When u reaches to $2.63 \times 10^{-3} \text{ mm}$, the first tensile cracks occurs around the left and right tips of the flaw ②. These two cracks are perpendicular to the direction of the applied displacement. In addition, the load reaches to the maximum as shown in Fig. 20. When the displacement u reaches to $2.64 \times 10^{-3} \text{ mm}$, the cracks from the tips of the flaw ② propagates perpendicular to u while the

load starts to drop after the peak load. Additionally, new cracks occur from the right tip of the flaw ① and the left tip of the flaw ③.

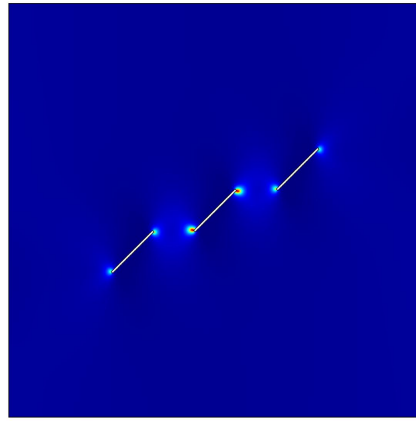
Figure 19(d) shows the coalescences of the cracks from the tips of the flaws ①, ②, and ③ when $u = 2.65 \times 10^{-3}$ mm. Thus, the flaw ② links the flaws ① and ③, which is accompanied by a sudden drop of the load after the maximum value in Fig. 20. At the same time, new cracks from the left tip of the flaw ① and the right tip of the flaw ③ are observed. When $u = 2.66 \times 10^{-3}$ mm, the cracks from the flaws ① and ③ continue to propagate and the load decreases. When the displacement increases to 2.69×10^{-3} mm, the cracks initiating from the left tip of the flaw ① and the right tip of the flaw ③ reach the boundaries of the rock sample. This indicates the rock loses its load-bearing capacity, which can also be verified by Fig. 20.

We now consider the same square rock sample subjected to tension with nine pre-existing flaws in Fig. 21. These flaws have the same inclination angle of 45° , while the lengths and spacing are not fixed. The position and geometry of the flaws are shown in Fig. 21. The parameters are the same as those in the example of three flaws. A total of 107982 6-node quadratic elements are used to discretize the rock sample and the maximum element size h is 0.25 mm. The displacement increment $\Delta u = 1 \times 10^{-6}$ mm is applied in each time step.

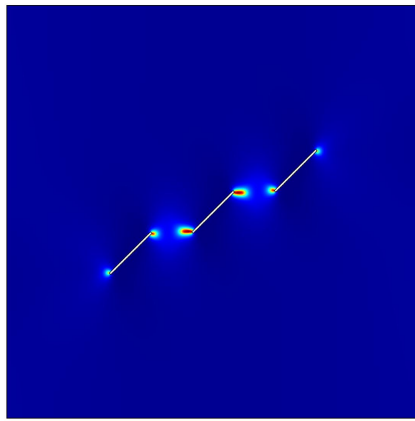
Figure 22(a)-(f) shows the propagation and coalescence process of the nine pre-existing flaws, and the reaction force on the upper boundary of the rock sample is depicted in Fig. 23. As the displacement u increases, the phase field around the tips of the flaws and the load both increase. The first tensile cracks initiate from the left tips of the flaws ⑧ and ⑨ when the displacement u reaches to 3.02×10^{-3} mm. At this time, the load achieves the maximum value. As the displacement increases to 3.04×10^{-3} mm, the crack from the left tip of the flaw ⑧ propagates and links up the flaw ⑦. The crack from the left tip of the flaw ⑨ continues to propagate while new cracks initiate from the left tip of the flaw ⑦ and the right tips of the flaws ⑧ and ⑨. The load then has a drop after the peak point (a). When u reaches to 3.06×10^{-3} mm and 3.08×10^{-3} mm, the cracks initiating from the left tip of the flaw ⑨ and the right tip of the flaw ⑧ continue to propagate at a decreasing rate and at a small angle with the horizontal. However, the cracks from the left tip of the flaw ⑦ and the right tip of the flaw ⑨ propagate at relatively large velocity nearly along the horizontal direction. The load decreases sharply as the applied displacement increases.



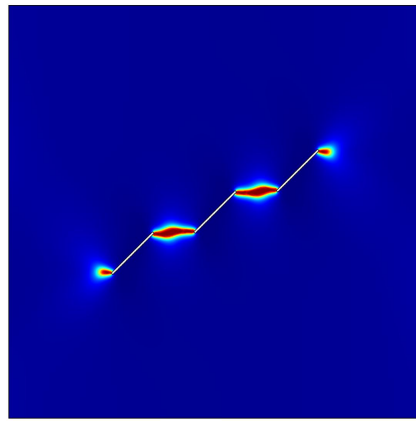
(a)



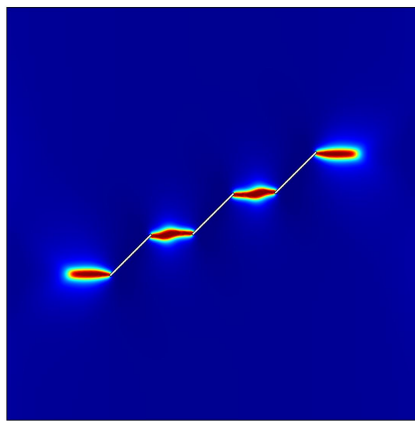
(b)



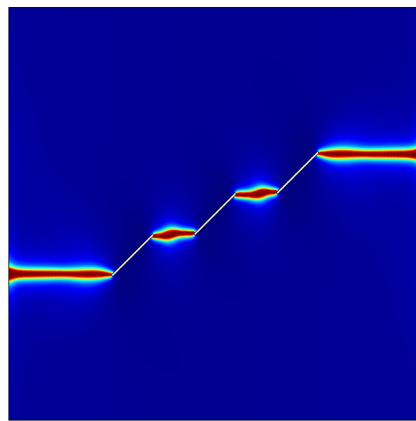
(c)



(d)



(e)



(f)

Figure 19: Propagation and coalescence of the three pre-existing flaws in a square rock sample at a displacement of (a) $u = 2.6 \times 10^{-3}$ mm, (b) $u = 2.63 \times 10^{-3}$ mm, (c) $u = 2.64 \times 10^{-3}$ mm, (d) $u = 2.65 \times 10^{-3}$ mm, (e) $u = 2.66 \times 10^{-3}$ mm, and (f) $u = 2.69 \times 10^{-3}$ mm

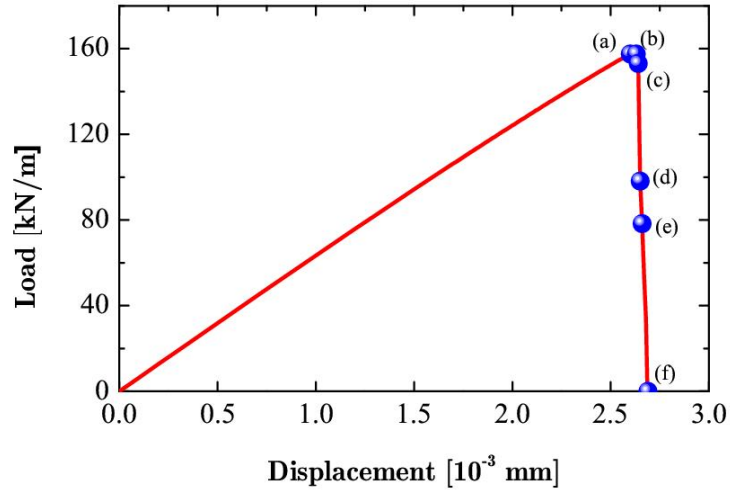


Figure 20: Load-displacement curves for the square rock sample with three pre-existing flaws

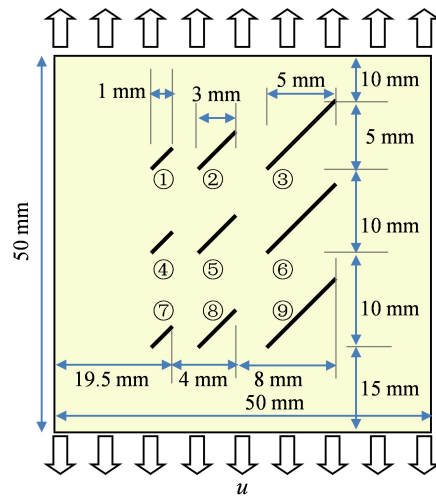


Figure 21: Geometry and boundary condition of nine pre-existing flaws

Figure 22(e) shows that the crack from the left tip of the flaw ⑦ propagates close to the left boundary of the rock sample when $u = 3.12 \times 10^{-3}$ mm. The crack initiating from the right tip of the flaw ⑨ propagates at a relatively small rate because of a larger distance from the boundary where the applied displacement is applied. When $u = 3.14 \times 10^{-3}$ mm, the cracks from the left tip of the flaw ⑦ and the right tip of the flaw ⑨ both reaches the left and right boundaries of the rock sample, indicating the failure of rock sample. The rock loses its load-bearing capacity and the load drops to near 0 in Fig. 23. In addition, Fig. 22 shows no cracks initiation from the tips of the flaws ①-⑥. The reason is the stress shielding and amplification effects due to the interaction of the flaws Zhou et al. (2015).

4.4 Propagation and coalescence of twenty parallel flaws

A 2D square rock sample with twenty parallel pre-existing flaws subjected to tension is tested. All flaws have the same length, spacing, and inclination angle of 0° . We consider the flaws in doubly periodic rectangular and diamond-shaped arrays, respectively. The arrangement and geometry of the flaws are depicted in Fig. 24. The rock sample are 50 mm \times 50 mm. These parameters are adopted: the rock density $\rho = 2450$ kg/m³, the Young's modulus $E = 30$ GPa, the Poisson's ratio $\nu = 0.3$, $G_c = 100$ J/m², $k = 1 \times 10^{-9}$, and the length scale $l_0 = 0.4$ mm. The rock sample is discretized by using uniform 8-node quadratic elements with the element size $h = 0.2$ mm. We adopt the displacement increment $\Delta u = 5 \times 10^{-6}$ mm for each time step.

Figure 25 presents the load-displacement curves for the square rock sample with twenty parallel flaws. A sudden drop of the load is also observed after the maximum value is obtained. Figure 26 presents the propagation and coalescence of the doubly periodic rectangular array of twenty pre-existing flaws. As the displacement u increases, the phase field ϕ concentrates at the tip of each flaw and the load achieves the maximum when $u = 2.185 \times 10^{-2}$ mm. When the displacement u reaches to 2.19×10^{-2} mm, the first tensile cracks initiate from the left and right tips of the flaws ①, ⑤, ⑰, and ⑳. In addition, the load has a small drop from the peak. When $u = 2.195 \times 10^{-2}$ mm, the first cracks continue to propagate perpendicular to the direction of the applied displacement and the load decreases. However, when $u = 2.2 \times 10^{-2}$ mm, the cracks fully connect the flaws ①, ⑤, ⑰, and ⑳ with the flaws ②, ③, ⑱, and ⑲. Moreover, some new cracks initiate from the right tips of the flaws ② and ⑱ as well as the left tips of the flaws ③ and

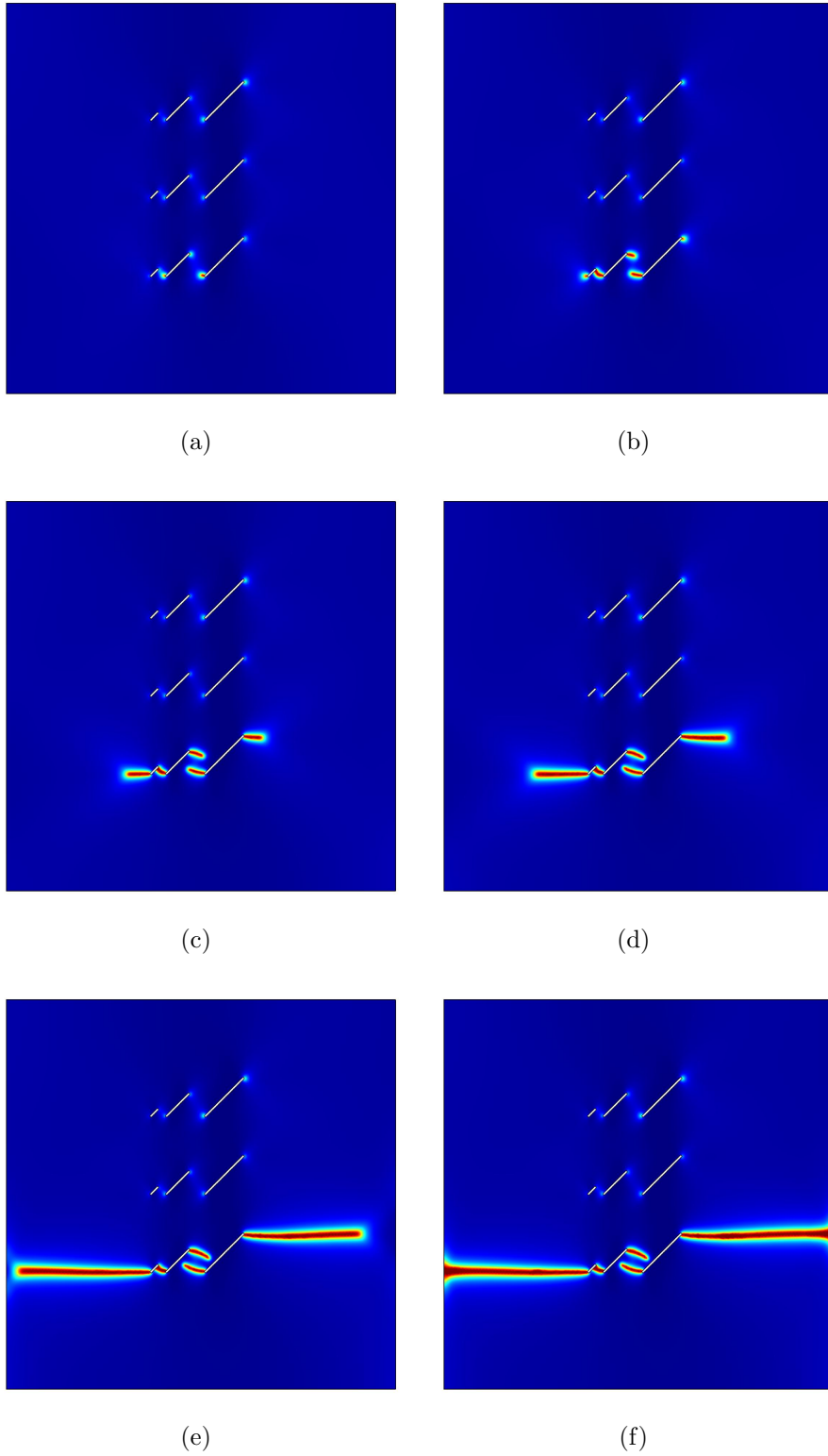


Figure 22: Propagation and coalescence of the nine pre-existing flaws in a square rock sample at a displacement of (a) $u = 3.02 \times 10^{-3}$ mm, (b) $u = 3.04 \times 10^{-3}$ mm, (c) $u = 3.06 \times 10^{-3}$ mm, (d) $u = 3.08 \times 10^{-3}$ mm, (e) $u = 3.12 \times 10^{-3}$ mm, and (f) $u = 3.14 \times 10^{-3}$ mm

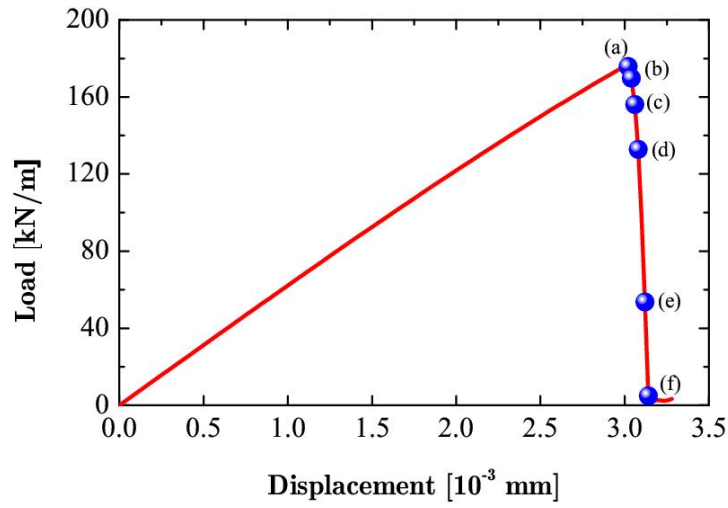


Figure 23: Load-displacement curves for the square rock sample with nine pre-existing flaws

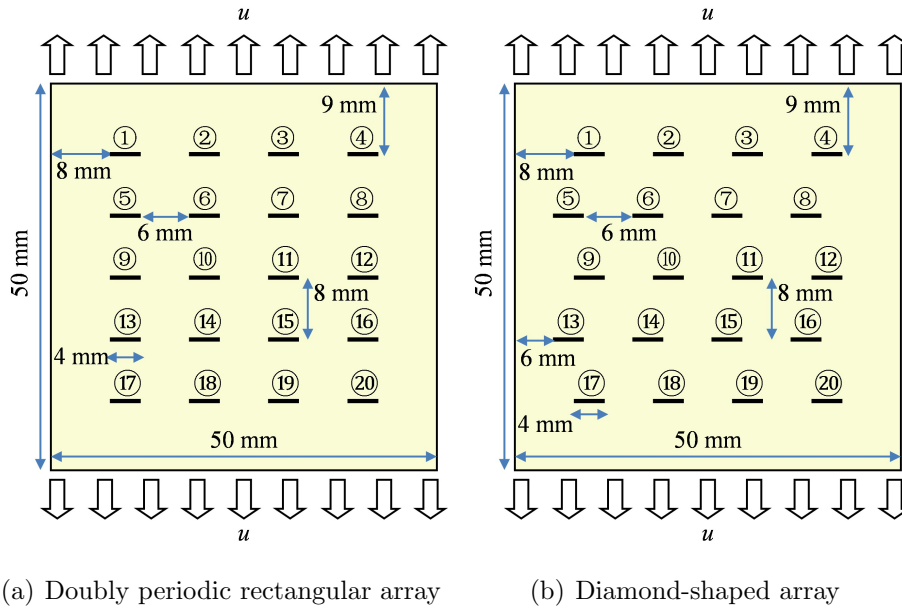
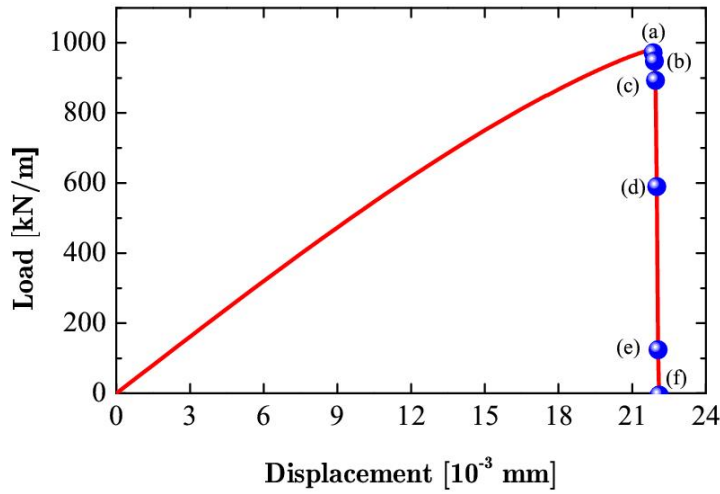
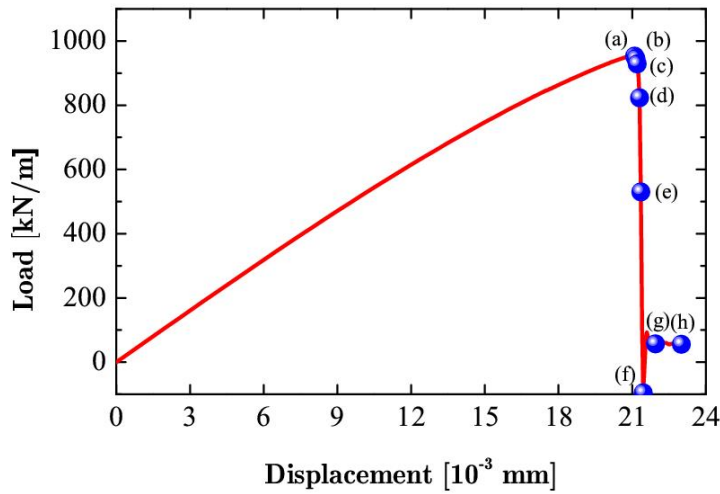


Figure 24: Arrangement and geometry of the twenty pre-existing flaws and the boundary condition

⑱. The load then drops to approximately 60% of the maximum load. When $u = 2.205 \times 10^{-2}$ mm, the cracks initiating from the right tips of the flaws ② and ⑱ and the cracks from the left tips of the flaws ③ and ⑲ coalesce. Finally, the cracks from the left tips of the flaws ① and ⑰ as well as the cracks from the right tips of the flaws ④ and ⑳ reach the left and right sides of the rock sample when $u = 2.21 \times 10^{-2}$ mm, indicating that the rock loses the load-bearing capacity. In addition, no cracks initiate from the tips of the flaws ⑤ - ⑯.



(a) Doubly periodic rectangular array



(b) Diamond-shaped array

Figure 25: Load-displacement curves for the square rock sample with twenty parallel pre-existing flaws

Figure 27 presents the propagation and coalescence of the twenty pre-existing flaws in the

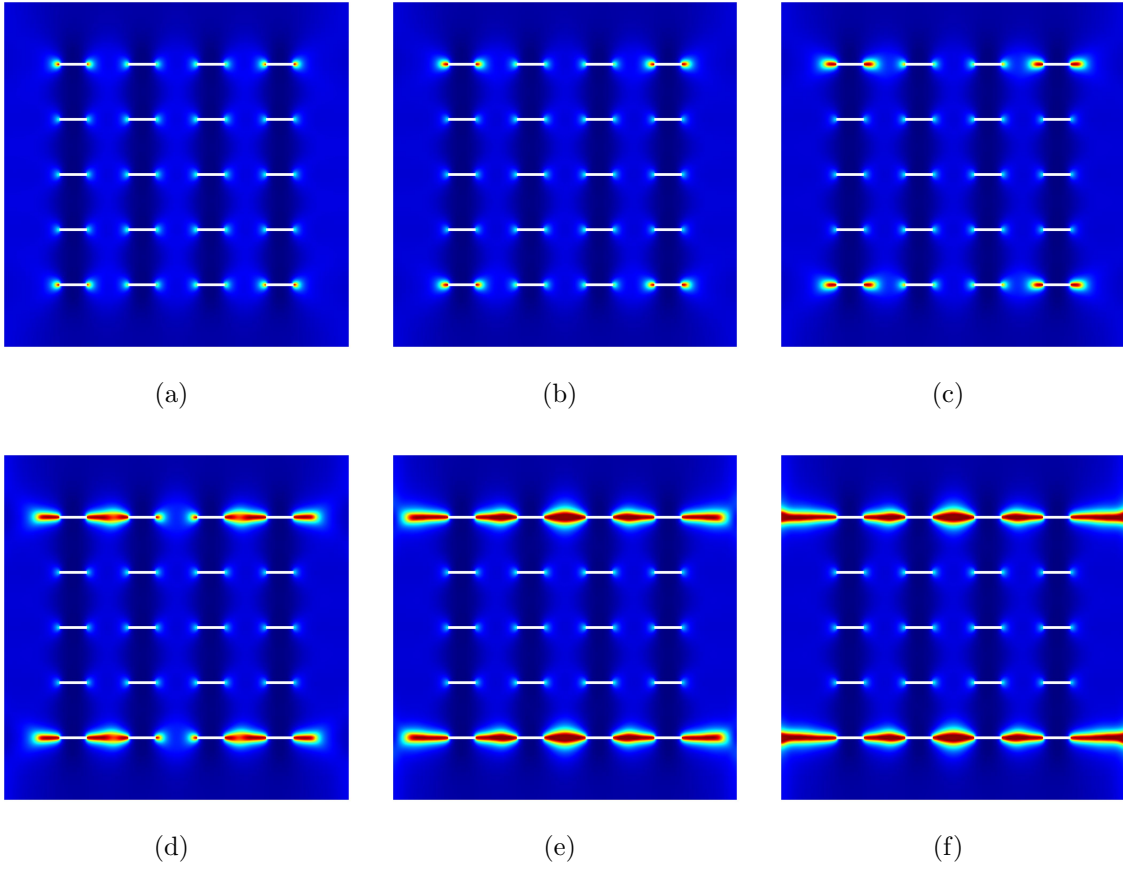


Figure 26: Propagation and coalescence of the doubly periodic rectangular array of twenty pre-existing flaws at a displacement of (a) $u = 2.185 \times 10^{-2}$ mm, (b) $u = 2.19 \times 10^{-2}$ mm, (c) $u = 2.195 \times 10^{-2}$ mm, (d) $u = 2.2 \times 10^{-2}$ mm, (e) $u = 2.205 \times 10^{-2}$ mm, and (f) $u = 2.21 \times 10^{-2}$ mm

diamond-shaped array. The crack patterns for the diamond-shaped array are different from those for the doubly periodic rectangular array. As the displacement u increases, the phase field ϕ rapidly increases around the tips closest to the left and right boundaries of the rock sample. When the displacement u reaches to 2.11×10^{-2} mm, the load increases to the maximum. When $u = 2.115 \times 10^{-2}$ mm, the tensile cracks first emanate from the left tips of the flaws ⑤ and ⑬ as well as the right tips of the flaws ④ and ⑳. When $u = 2.12 \times 10^{-2}$ mm, another two cracks initiate from the left tips of the flaws ④ and ⑳. The first four cracks continue to propagate along the horizontal direction, while the load at $u = 2.12 \times 10^{-2}$ mm is close to that at $u = 2.11 \times 10^{-2}$ mm and $u = 2.115 \times 10^{-2}$ mm.

The flaws close to the top and bottom edges of the sample are placed perpendicular to the direction of loading. The arrangement of the internal flaws has little effect on the propagation of the edge flaws. Therefore, cracks propagating from those edge flaws will show typical features of Mode-I fracture. As shown in Fig. 27, when $u = 2.130 \times 10^{-2}$ mm, the originally initiating cracks propagate as expected, while new cracks emanate from the right tips of the flaws ③, ⑤, ⑬, and ⑱. The load then starts to drop from the peak region. However, when $u = 2.135 \times 10^{-2}$ mm, the cracks fully connect the flaws ③ and ⑱ with the flaws ④ and ⑳. In addition, two new cracks initiate from the left tips of the flaws ③ and ⑱. At this time, the load decreases to approximately half of the peak load. As the displacement u increases to 2.145×10^{-2} mm, the propagating cracks and the flaws ②, ③, ⑤, ⑥, ⑬, ⑭, ⑱, and ⑲ coalesce. At the same time, the cracks from the left tips of the flaws ⑤ and ⑬ as well as the cracks from the right tips of the flaws ④ and ⑳ reach the left and right sides of the rock sample. The load at $u = 2.145$ mm is less than zero followed by new cracks emanating from the left tip of the flaw ② and the right tip of the flaw ⑥.

When the displacement u reaches to 2.195×10^{-2} mm and 2.3×10^{-2} mm, the crack initiating from the right tip of the flaw ⑭ slowly propagates; however, the cracks from the left tip of the flaw ② and the right tip of the flaw ⑥ continue to propagate obliquely at a relatively large velocity. The difference in the crack patterns from Figs. 26 and 27 implies that initiation, propagation and coalescence of the cracks are significantly affected by the arrangement of the flaws.

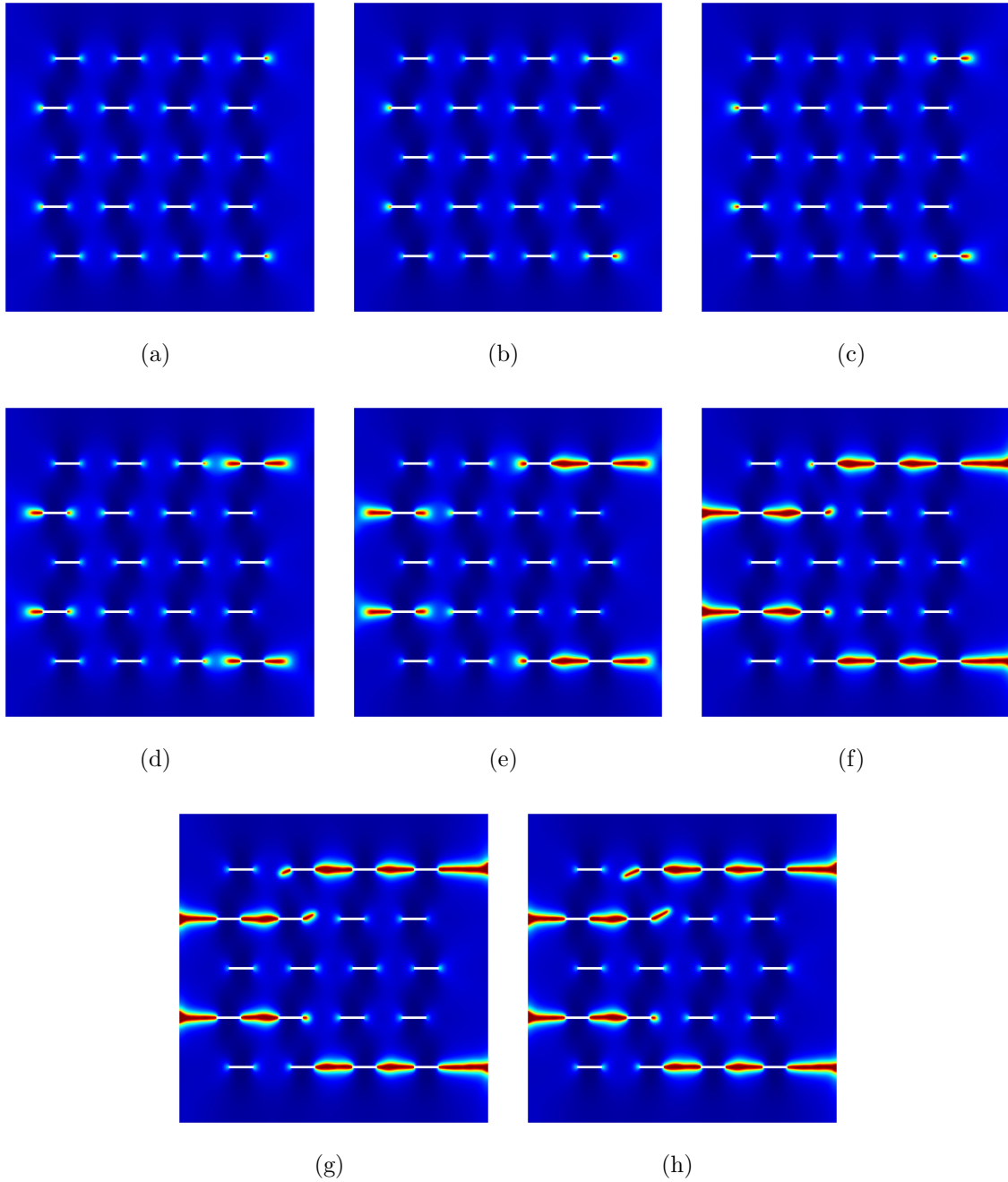


Figure 27: Propagation and coalescence of the diamond-shaped array of twenty pre-existing flaws at a displacement of (a) $u = 2.11 \times 10^{-2}$ mm, (b) $u = 2.115 \times 10^{-2}$ mm, (c) $u = 2.120 \times 10^{-2}$ mm, (d) $u = 2.130 \times 10^{-2}$ mm, (e) $u = 2.135 \times 10^{-2}$ mm, (f) $u = 2.145 \times 10^{-2}$ mm, (g) $u = 2.195 \times 10^{-2}$ mm, and (h) $u = 2.3 \times 10^{-2}$ mm

4.5 Crack branching in a plate subjected to internal pressure

This example is a square plate subjected to internal pressure with geometry and boundary conditions shown in Fig. 28. The internal pressure is applied on the upper and lower boundaries of the notch with $\bar{p} = 1 \text{ MPa/s}$, while the outer boundaries of the plate are traction-free. In this example, dynamic cracks are considered, and these parameters are adopted: the rock density $\rho = 2450 \text{ kg/m}^3$, the Poisson's ratio $\nu = 0.3$, $G_c = 1 \text{ J/m}^2$, $k = 1 \times 10^{-9}$, and the length scale $l_0 = 0.4 \text{ mm}$. The plate is discretized by using uniform Q4 elements with the element size $h = l_0$, and we adopt the time step size $\Delta t = 0.01 \text{ } \mu\text{s}$.

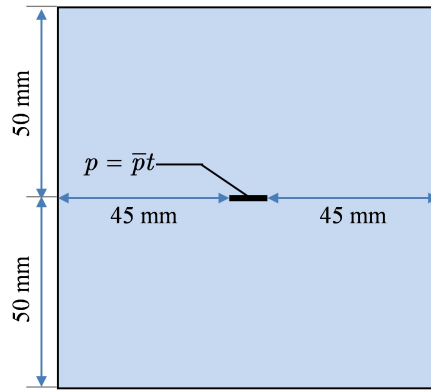


Figure 28: Geometry and boundary conditions of the plate subjected to internal pressure

We consider the plate as a heterogeneous material and apply a Weibull distribution to the Young's modulus:

$$\varphi(E) = \frac{m}{E_0} \left(\frac{E}{E_0} \right)^{m-1} \exp \left(- \frac{E}{E_0} \right)^m \quad (40)$$

where φ is the probability density function and coefficient m determines the shape of φ . m also reflects the homogeneity of the material. As m increases, the material becomes more homogeneous and vice versa. In this paper, we consider $m = 1, 3, 5, 7$, and 9 along with $m = \infty$ representing a homogeneous plate. We use $E_0 = 30 \text{ GPa}$ and Fig. 29 shows the distribution of Young's modulus for different m .

Figure 30 presents the crack patterns of the plate subjected to internal pressure for different m . Complex crack patterns, such as many crack branching, are observed. These observations are different from the previous examples. When the time t reaches $20 \text{ } \mu\text{s}$, cracks initiate from the left and right tips of the notch and then start to branch. When the time t increases to

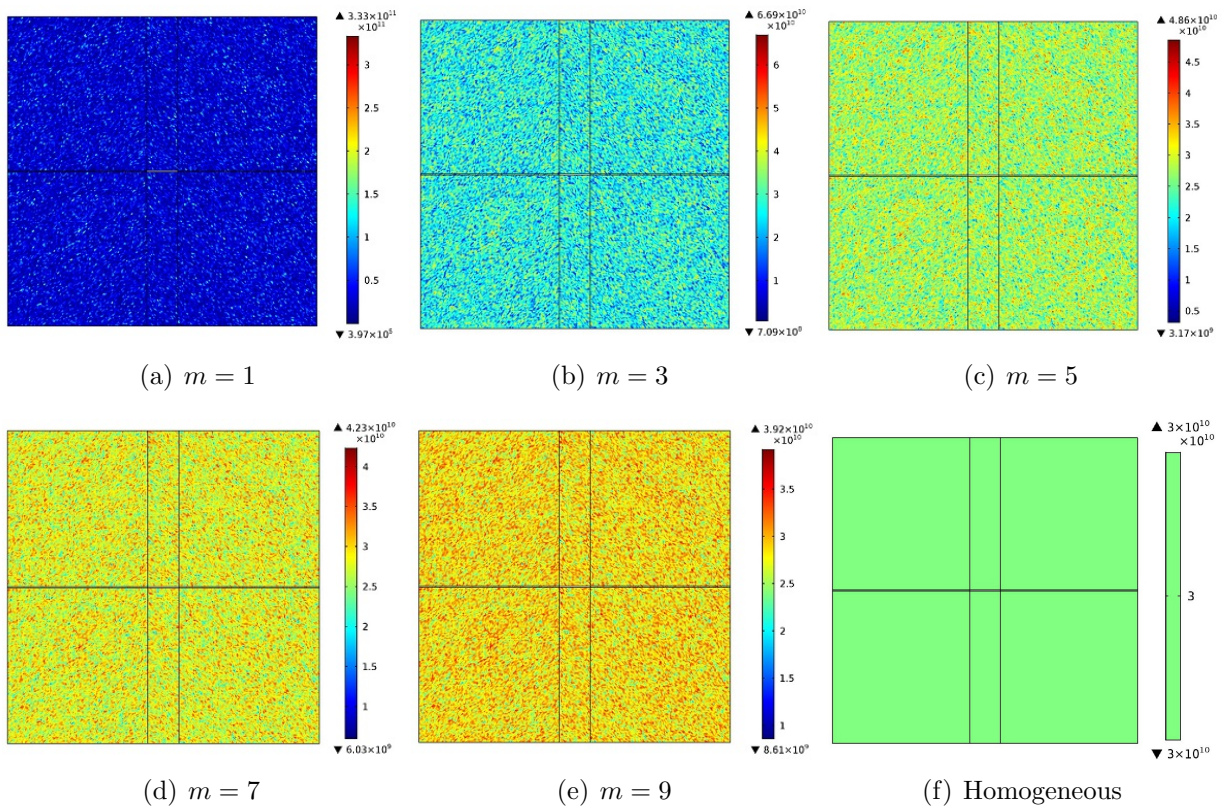


Figure 29: Young's modulus of the plate

30 μs , the branching cracks propagate. When $t = 50\mu s$, large “damage” region are observed around the notch where ϕ is large. At $t = 60 \mu s$, some cracks initiate from the upper and lower boundaries of the plate, while the cracks from the notch keep propagating. Finally, when $t = 70 \mu s$, many new cracks occur inside the plate and the cracks from the upper and lower boundaries of the plate start to branch. For a smaller m , more crack branching is observed during the crack propagation. Therefore, a smaller m produces more complex crack patterns.

4.6 3D Petersson beam

In this example, the phase field model is applied to a single edge notched beam subjected to three-point bending (the so-called Petersson beam). A 3D simulation is conducted in this example. The geometry and boundary conditions are depicted in Fig. 31 according to Petersson (1981). The thickness of the beam is 50 mm. The following mechanical properties of the beam are chosen Petersson (1981): Young’s modulus $E = 27$ GPa, Poisson’s ratio $\nu = 0.21$, critical energy release rate $G_c = 56$ J/m² and length scale $l_0 = 1$ mm. We choose the maximum element size $h = 5$ mm in most of the beam but $h = 1$ mm in the region where the crack is expected to propagate. A displacement increment of $\Delta u = 2.5 \times 10^{-4}$ mm is used.

Figure 32 compares the load-displacement curves obtained of the phase field model with the experimental test (Petersson 1981). The results obtained by the phase field model are in good agreement with the experimental test. Figure 33 presents the crack propagation in the beam at the displacements $u = 0.34$ mm, 0.355 mm, and 0.46 mm.

4.7 3D NSCB tests

In the last example, we simulate the crack propagation in a 3D NSCB specimen. The geometry and boundary conditions are similar to the 2D tests except a thickness of 16 mm in 3D. The same parameters are used as those in the 2D tests and $G_c = 7.6$ J/m². We refine the elements with the maximum size $h = 4.5 \times 10^{-4}$ m in the region where the crack is expected to propagate, while in the rest region $h = 1.8 \times 10^{-3}$ m. In addition, the displacement increment $\Delta u = 5 \times 10^{-7}$ mm is applied.

Figure 34 presents the crack propagation at the displacements $u = 6.67 \times 10^{-3}$ mm, 6.71×10^{-3}

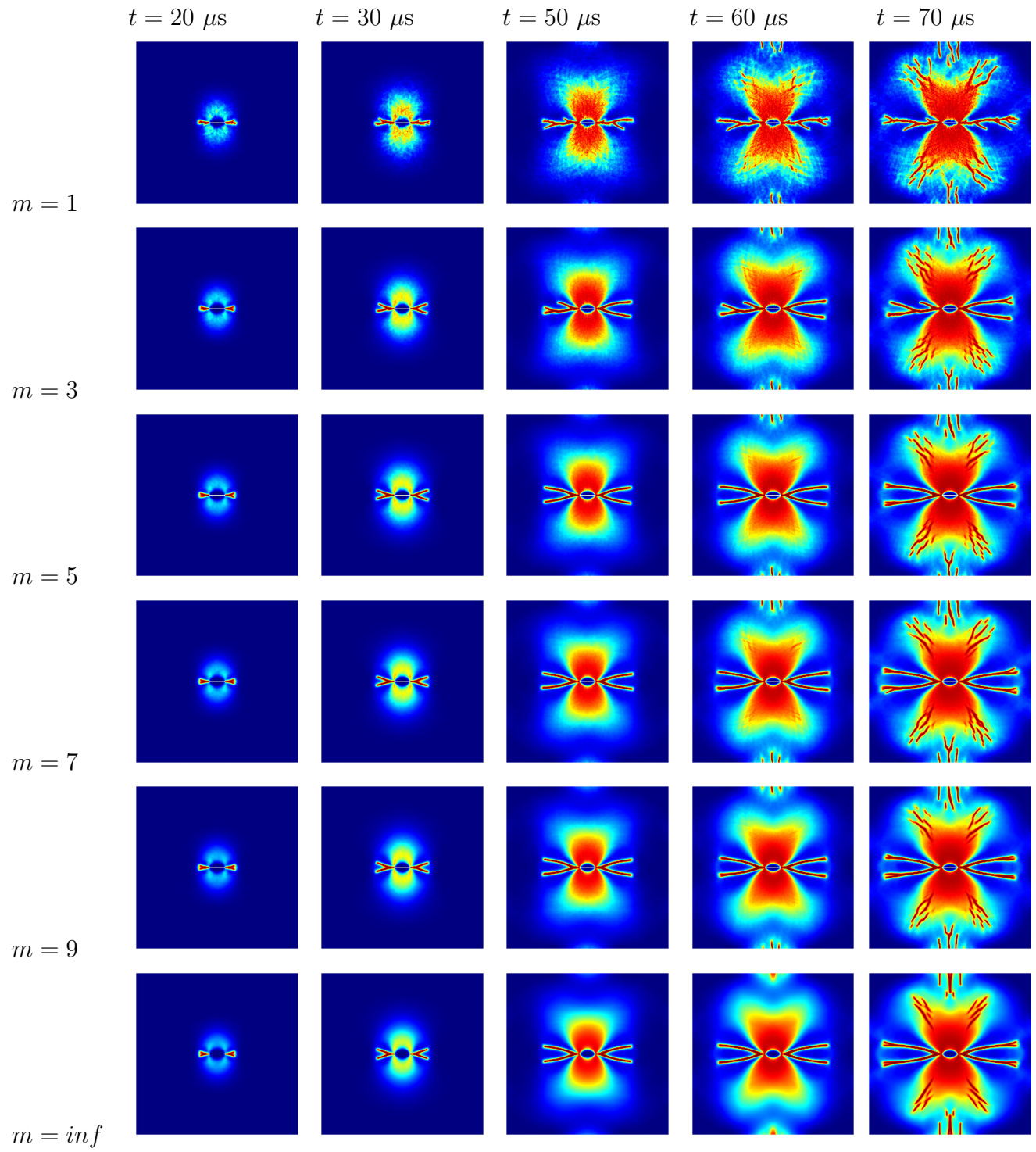


Figure 30: Crack patterns of the plate subjected to internal pressure

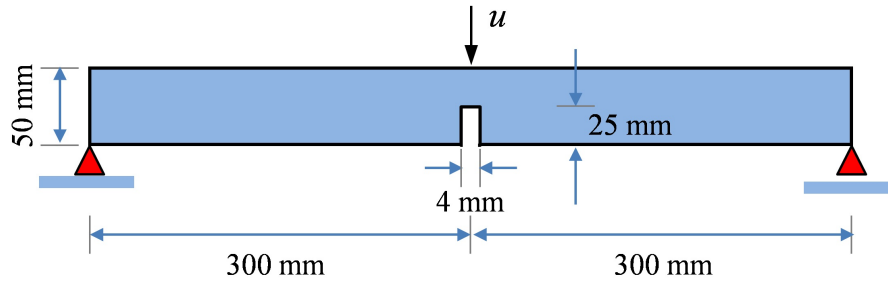


Figure 31: Geometry and boundary condition of Petersons beam

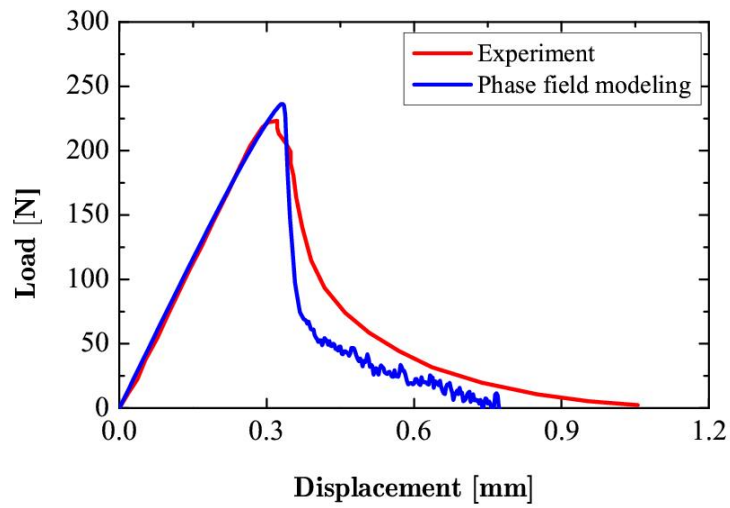
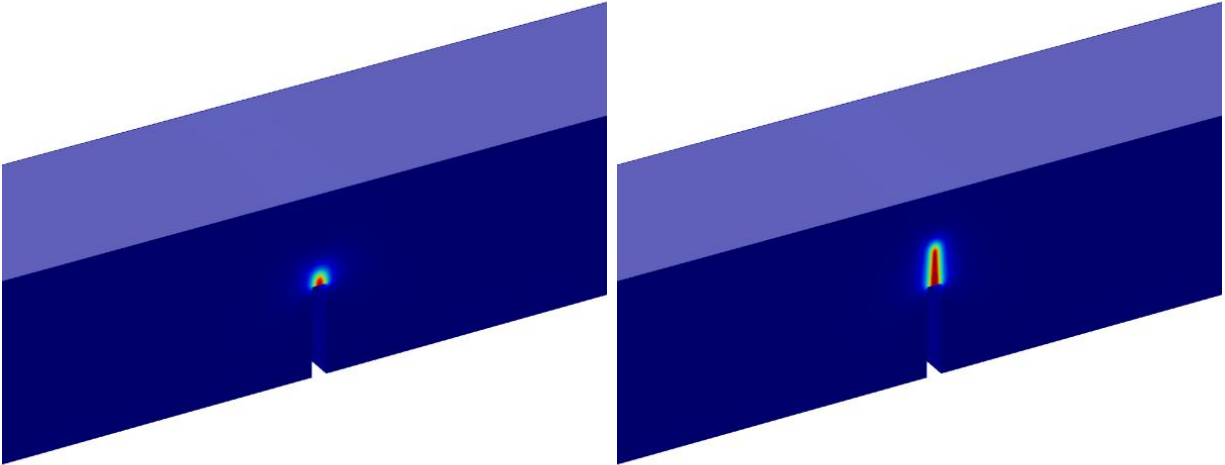
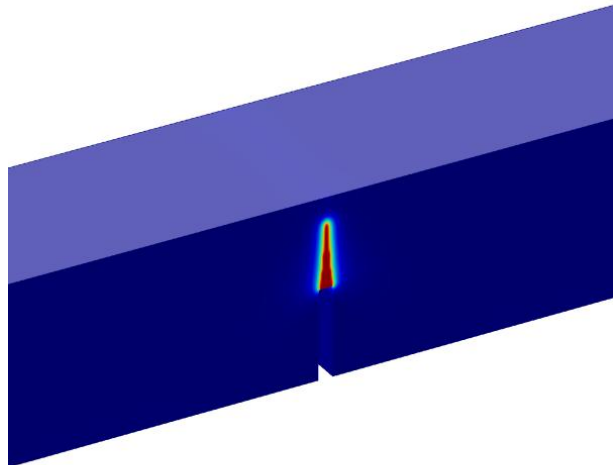


Figure 32: Load-displacement curves of 3D petersson beam



(a)

(b)



(c)

Figure 33: Crack propagation in the 3D pettersson beam at a displacement of (a) $u = 0.34$ mm, (b) $u = 0.355$ mm, and (c) $u = 0.46$ mm

mm, and 6.745×10^{-3} mm. Only the domain with $\phi > 0.95$ are displayed for the crack shape. The crack patterns are the same as those in the 2D simulation, and also in good agreement with the results of the experimental tests (Gao et al. 2015). The example of 3D NSCB test shows the ability and practicability of the phase field method in modeling crack propagation of rocks in 3D.

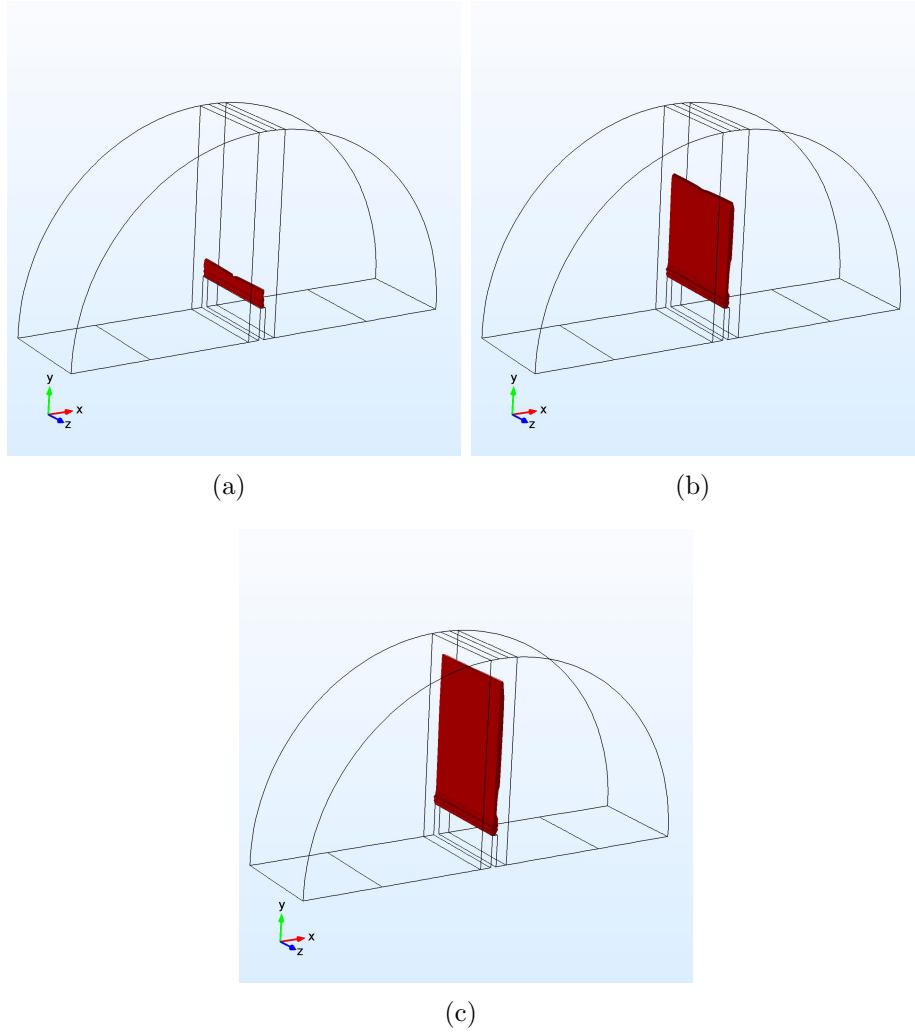


Figure 34: Crack propagation of the 3D NSCB test at a displacement of (a) $u = 6.67 \times 10^{-3}$ mm, (b) $u = 6.71 \times 10^{-3}$ mm, and (c) $u = 6.745 \times 10^{-3}$ mm for $G_c = 7.6 \text{ J/m}^2$

5 Conclusions

The phase field theory for fracture is applied to study the crack propagation, branching and coalescence in rocks. Implementation details of the phase field modeling in COMSOL are presented with the consideration of cracks only due to tension. The numerical simulations of the 2D notched semi-circular bend (NSCB) tests and Brazil splitting tests are then performed. The presented results are in good agreement with those of the previous experimental tests. Subsequently, the crack propagation and coalescence in plates with multiple echelon flaws and twenty parallel flaws are studied. We also present the complex crack patterns in a plate subjected to internal pressure, the increase of which produces crack propagation and branching. Finally, the simulation of a 3D Petersson beam and a 3D NSCB test are performed to show the practicability of phase field modeling in 3D rocks.

All the numerical examples presented by this work show that the initiation, propagation, coalescence, and branching of cracks are autonomous, while the phase field modeling does not require external criterion for fracture and setting propagation path in advance. These observations highlight the advantages of the phase field method over other numerical methods in modeling complex crack propagation in rocks. Therefore, the phase field modeling approach will be useful and practicable for other crack problems in rock engineering in future research. In addition, the presented phase field model cannot predict the shear cracks when a rock reaches its shear strength. The reason is that the shear strength is not involved in the formulation of the phase field method and the crack propagation is only driven by the elastic energy. In this sense, a modified phase field model coupled with the shear model of rocks will be also attractive in the future.

Acknowledgement

The financial support provided by the Sino-German (CSC-DAAD) Postdoc Scholarship Program 2016, the Natural Science Foundation of China (51474157), and RISE-project BESTOFRAC (734370) is gratefully acknowledged.

References

- Ted L Anderson. *Fracture mechanics: fundamentals and applications*. CRC press, 2005.
- Antonio Bobet and HH Einstein. Fracture coalescence in rock-type materials under uniaxial and biaxial compression. *International Journal of Rock Mechanics and Mining Sciences*, 35(7): 863–888, 1998.
- RHC Wong, KT Chau, CA Tang, and P Lin. Analysis of crack coalescence in rock-like materials containing three flaws part i: experimental approach. *International Journal of Rock Mechanics and Mining Sciences*, 38(7):909–924, 2001.
- M Sagong and A Bobet. Coalescence of multiple flaws in a rock-model material in uniaxial compression. *International Journal of Rock Mechanics and Mining Sciences*, 39(2):229–241, 2002.
- LNW Wong and HH Einstein. Crack coalescence in molded gypsum and carrara marble: part 1. macroscopic observations and interpretation. *Rock Mechanics and Rock Engineering*, 42(3): 475–511, 2009.
- CH Park and A Bobet. Crack coalescence in specimens with open and closed flaws: a comparison. *International Journal of Rock Mechanics and Mining Sciences*, 46(5):819–829, 2009.
- CH Park and A Bobet. Crack initiation, propagation and coalescence from frictional flaws in uniaxial compression. *Engineering Fracture Mechanics*, 77(14):2727–2748, 2010.
- Heekwang Lee and Seokwon Jeon. An experimental and numerical study of fracture coalescence in pre-cracked specimens under uniaxial compression. *International Journal of Solids and Structures*, 48(6):979–999, 2011.
- XP Zhou, H Cheng, and YF Feng. An experimental study of crack coalescence behaviour in rock-like materials containing multiple flaws under uniaxial compression. *Rock mechanics and rock engineering*, 47(6):1961–1986, 2014.

- P. Areias and T. Rabczuk. Steiner-point free edge cutting of tetrahedral meshes with applications in fracture. *Finite Elements in Analysis and Design*, 132:27–41, 2017. doi: 10.1016/j.finel.2017.05.001.
- P. Areias, T. Rabczuk, and D. Dias-da Costa. Element-wise fracture algorithm based on rotation of edges. *Engineering Fracture Mechanics*, 110:113–137, 2013. doi: 10.1016/j.engfracmech.2013.06.006.
- P. Areias and T. Rabczuk. Finite strain fracture of plates and shells with configurational forces and edge rotations. *International Journal for Numerical Methods in Engineering*, 94(12):1099–1122, 2013. doi: 10.1002/nme.4477.
- Pattabhi R Budarapu, Robert Gracie, Stéphane PA Bordas, and Timon Rabczuk. An adaptive multiscale method for quasi-static crack growth. *Computational Mechanics*, 53(6):1129–1148, 2014a.
- Pattabhi R Budarapu, Robert Gracie, Shih-Wei Yang, Xiaoying Zhuang, and Timon Rabczuk. Efficient coarse graining in multiscale modeling of fracture. *Theoretical and Applied Fracture Mechanics*, 69:126–143, 2014b.
- Shih-Wei Yang, Pattabhi R Budarapu, D Roy Mahapatra, Stéphane PA Bordas, Goangseup Zi, and Timon Rabczuk. A meshless adaptive multiscale method for fracture. *Computational Materials Science*, 96:382–395, 2015.
- P. Areias, T. Rabczuk, and P.P. Camanho. Finite strain fracture of 2d problems with injected anisotropic softening elements. *Theoretical and Applied Fracture Mechanics*, 72(1):50–63, 2014. doi: 10.1016/j.tafmec.2014.06.006.
- SS Nanthakumar, Tom Lahmer, and Timon Rabczuk. Detection of multiple flaws in piezoelectric structures using xfem and level sets. *Computer Methods in Applied Mechanics and Engineering*, 275:98–112, 2014.
- Nicolas Moës and Ted Belytschko. Extended finite element method for cohesive crack growth. *Engineering fracture mechanics*, 69(7):813–833, 2002.

- Timon Rabczuk, Goangseup Zi, Axel Gerstenberger, and Wolfgang A Wall. A new crack tip element for the phantom-node method with arbitrary cohesive cracks. *International Journal for Numerical Methods in Engineering*, 75(5):577–599, 2008a.
- Thanh Chau-Dinh, Goangseup Zi, Phill-Seung Lee, Timon Rabczuk, and Jeong-Hoon Song. Phantom-node method for shell models with arbitrary cracks. *Computers & Structures*, 92: 242–256, 2012.
- Nam Vu-Bac, Hung Nguyen-Xuan, Lei Chen, Chang-Kye Lee, Goangseup Zi, X Zhuang, Gui Rong Liu, and Timon Rabczuk. A phantom-node method with edge-based strain smoothing for linear elastic fracture mechanics. *Journal of Applied Mathematics*, 2013, 2013.
- Timon Rabczuk, PMA Areias, and Ted Belytschko. A simplified mesh-free method for shear bands with cohesive surfaces. *International Journal for Numerical Methods in Engineering*, 69(5):993–1021, 2007a.
- Timon Rabczuk and Goangseup Zi. A meshfree method based on the local partition of unity for cohesive cracks. *Computational Mechanics*, 39(6):743–760, 2007.
- Timon Rabczuk, Stéphane Bordas, and Goangseup Zi. A three-dimensional meshfree method for continuous multiple-crack initiation, propagation and junction in statics and dynamics. *Computational Mechanics*, 40(3):473–495, 2007b.
- T Rabczuk and E Samaniego. Discontinuous modelling of shear bands using adaptive meshfree methods. *Computer Methods in Applied Mechanics and Engineering*, 197(6):641–658, 2008.
- Timon Rabczuk, Goangseup Zi, Stéphane Bordas, and Hung Nguyen-Xuan. A geometrically non-linear three-dimensional cohesive crack method for reinforced concrete structures. *Engineering Fracture Mechanics*, 75(16):4740–4758, 2008b.
- F. Amiri, C. Anitescu, M. Arroyo, S.P.A. Bordas, and T. Rabczuk. Xlme interpolants, a seamless bridge between xfem and enriched meshless methods. *Computational Mechanics*, 53(1):45–57, 2014a. doi: 10.1007/s00466-013-0891-2.

- T. Rabczuk and T. Belytschko. Cracking particles: A simplified meshfree method for arbitrary evolving cracks. *International Journal for Numerical Methods in Engineering*, 61(13):2316–2343, 2004. doi: 10.1002/nme.1151.
- T. Rabczuk and T. Belytschko. A three-dimensional large deformation meshfree method for arbitrary evolving cracks. *Computer Methods in Applied Mechanics and Engineering*, 196(29-30):2777–2799, 2007. doi: 10.1016/j.cma.2006.06.020.
- Timon Rabczuk, Goangseup Zi, Stephane Bordas, and Hung Nguyen-Xuan. A simple and robust three-dimensional cracking-particle method without enrichment. *Computer Methods in Applied Mechanics and Engineering*, 199(37):2437–2455, 2010.
- Timon Rabczuk and Huilong Ren. A peridynamics formulation for quasi-static fracture and contact in rock. *Engineering Geology*, 2017.
- Huilong Ren, Xiaoying Zhuang, Yongchang Cai, and Timon Rabczuk. Dual-horizon peridynamics. *International Journal for Numerical Methods in Engineering*, 108(12):1451–1476, 2016.
- Huilong Ren, Xiaoying Zhuang, and Timon Rabczuk. Dual-horizon peridynamics: A stable solution to varying horizons. *Computer Methods in Applied Mechanics and Engineering*, 318:762–782, 2017.
- Ted Belytschko and Jerry I Lin. A three-dimensional impact-penetration algorithm with erosion. *International Journal of Impact Engineering*, 5(1-4):111–127, 1987.
- Gordon R Johnson and Robert A Stryk. Eroding interface and improved tetrahedral element algorithms for high-velocity impact computations in three dimensions. *International Journal of Impact Engineering*, 5(1-4):411–421, 1987.
- Jeong-Hoon Song, Hongwu Wang, and Ted Belytschko. A comparative study on finite element methods for dynamic fracture. *Computational Mechanics*, 42(2):239–250, 2008.
- Tran Quoc Thai, Timon Rabczuk, Yuri Bazilevs, and Günther Meschke. A higher-order stress-based gradient-enhanced damage model based on isogeometric analysis. *Computer Methods in Applied Mechanics and Engineering*, 304:584–604, 2016.

- Gilles Pijaudier-Cabot, Khalil Haidar, and Jean-François Dubé. Non-local damage model with evolving internal length. *International journal for numerical and analytical methods in geomechanics*, 28(7-8):633–652, 2004.
- P. Areias, M.A. Msekh, and T. Rabczuk. Damage and fracture algorithm using the screened poisson equation and local remeshing. *Engineering Fracture Mechanics*, 158:116–143, 2016a. doi: 10.1016/j.engfracmech.2015.10.042.
- Blaise Bourdin, Gilles A Francfort, and Jean-Jacques Marigo. The variational approach to fracture. *Journal of elasticity*, 91(1):5–148, 2008.
- Christian Miehe, Martina Hofacker, and Fabian Welschinger. A phase field model for rate-independent crack propagation: Robust algorithmic implementation based on operator splits. *Computer Methods in Applied Mechanics and Engineering*, 199(45):2765–2778, 2010a.
- C Miehe, F Welschinger, and M Hofacker. Thermodynamically consistent phase-field models of fracture: Variational principles and multi-field fe implementations. *International Journal for Numerical Methods in Engineering*, 83(10):1273–1311, 2010b.
- C Hesch and K Weinberg. Thermodynamically consistent algorithms for a finite-deformation phase-field approach to fracture. *International Journal for Numerical Methods in Engineering*, 99(12):906–924, 2014.
- Michael J Borden, Clemens V Verhoosel, Michael A Scott, Thomas JR Hughes, and Chad M Landis. A phase-field description of dynamic brittle fracture. *Computer Methods in Applied Mechanics and Engineering*, 217:77–95, 2012.
- P. Areias, T. Rabczuk, and M.A. Msekh. Phase-field analysis of finite-strain plates and shells including element subdivision. *Computer Methods in Applied Mechanics and Engineering*, 312:322–350, 2016b. doi: 10.1016/j.cma.2016.01.020.
- Fatemeh Amiri, Daniel Millán, Yongxing Shen, Timon Rabczuk, and M Arroyo. Phase-field modeling of fracture in linear thin shells. *Theoretical and Applied Fracture Mechanics*, 69: 102–109, 2014b. doi: 10.1016/j.tafmec.2013.12.002.

- Mohammed A Msekh, Juan Michael Sargado, Mostafa Jamshidian, Pedro Miguel Areias, and Timon Rabczuk. Abaqus implementation of phase-field model for brittle fracture. *Computational Materials Science*, 96:472–484, 2015.
- Guowei Liu, Qingbin Li, Mohammed A Msekh, and Zheng Zuo. Abaqus implementation of monolithic and staggered schemes for quasi-static and dynamic fracture phase-field model. *Computational Materials Science*, 121:35–47, 2016.
- Blaise Bourdin, Gilles A Francfort, and Jean-Jacques Marigo. Numerical experiments in revisited brittle fracture. *Journal of the Mechanics and Physics of Solids*, 48(4):797–826, 2000.
- Xue Zhang, Chet Vignes, Scott W Sloan, and Daichao Sheng. Numerical evaluation of the phase-field model for brittle fracture with emphasis on the length scale. *Computational Mechanics*, 59(5):737–752, 2017.
- C Miehe. Computation of isotropic tensor functions. *International Journal for Numerical Methods in Biomedical Engineering*, 9(11):889–896, 1993.
- Alex Toth and CT Kelley. Convergence analysis for anderson acceleration. *SIAM Journal on Numerical Analysis*, 53(2):805–819, 2015.
- G Gao, S Huang, K Xia, and Z Li. Application of digital image correlation (DIC) in dynamic notched semi-circular bend (NSCB) tests. *Experimental Mechanics*, 55(1):95–104, 2015.
- M Cai. Fracture initiation and propagation in a brazilian disc with a plane interface: a numerical study. *Rock mechanics and rock engineering*, 46(2):289–302, 2013.
- Xiao-Ping Zhou and Yun-Teng Wang. Numerical simulation of crack propagation and coalescence in pre-cracked rock-like brazilian disks using the non-ordinary state-based peridynamics. *International Journal of Rock Mechanics and Mining Sciences*, 89:235–249, 2016.
- C Atkinson, RE Smelser, and Jo Sanchez. Combined mode fracture via the cracked brazilian disk test. *International Journal of Fracture*, 18(4):279–291, 1982.
- Martin Entacher, E Schuller, and R Galler. Rock failure and crack propagation beneath disc cutters. *Rock Mechanics and Rock Engineering*, 48(4):1559–1572, 2015.

- N Erarslan and DJ Williams. Investigating the effect of cyclic loading on the indirect tensile strength of rocks. *Rock mechanics and rock engineering*, 45(3):327–340, 2012.
- Xiao-Ping Zhou, Xin-Bao Gu, and Yun-Teng Wang. Numerical simulations of propagation, bifurcation and coalescence of cracks in rocks. *international journal of Rock Mechanics and Mining Sciences*, 80:241–254, 2015.
- Per-Erik Petersson. Crack growth and development of fracture zones in plain concrete and similar materials. *Report TVBM 1006*, 1981.